AGU ADVANCING EARTH AND SPACE SCIENCE

JGR Solid Earth

RESEARCH ARTICLE

10.1029/2021JB022174

Complex Migration of Tremor Near Cholame, CA, Resolved by Seismic Array Analysis

A. Inbal[1], **A. M. Thomas**[2], **T. Newton**[2], **and R. Bürgmann**[3]

[1]Department of Geophysics, Tel Aviv University, Tel Aviv, Israel, [2]Department of Earth Sciences, University of Oregon, Eugene, OR, USA, [3]Department of Earth and Planetary Science, UC Berkeley, Berkeley, CA, USA

Key Points:

- Tremor is observed by dense seismic arrays deployed near Cholame, CA
- Long- and short-term migration speeds inferred from precisely located tremor are observed to vary by over three orders of magnitude
- We provide the first evidence for Rapid Tremor Reversals (RTR) occurring on the San Andreas Fault

Supporting Information:

Supporting Information may be found in the online version of this article.

Correspondence to:

A. Inbal,
asafinbal@tauex.tau.ac.il

Citation:

Inbal, A., Thomas, A. M., Newton, T., & Bürgmann, R. (2021). Complex migration of tremor near Cholame, CA, resolved by seismic array analysis. *Journal of Geophysical Research: Solid Earth*, *126*, e2021JB022174. https://doi.org/10.1029/2021JB022174

Received 4 APR 2021
Accepted 2 SEP 2021

Abstract

Tectonic tremor observed along the Cholame and Parkfield sections of the San Andreas Fault has previously been associated with transient slip beneath the seismogenic zone. To study tremor and associated Low Frequency Earthquakes (LFEs), we deployed three dense near-fault seismic arrays for a period of 3 months in 2018. In early August 2018, the arrays recorded a strong 4-day-long deep transient that nucleated in Cholame and propagated toward the northwest. The initiation area is characterized by tremor that persists throughout the transient, while adjacent fault portions located to the northwest host more intermittent tremor. From the rate and location of tremor and LFEs, we infer a deep slip transient, whose along-strike propagation velocity is ~8 km/day. Secondary tremor fronts are observed to travel ahead of the main slow slip front at speeds that are $10^2 - 10^3$ times faster. These rapid migrations propagate in slow slip events (SSE) slip-parallel direction, and are sometimes observed to back-propagate into previously ruptured segments. High-resolution images of secondary fronts obtained by using near-fault borehole stations indicate the active tremor band takes the shape of a narrow strain pulse that is bounded from above by the lower edge of the seismogenic zone. We estimate the stress drops associated with the secondary slip fronts are of the order of a few kPa. Frequency-dependent analysis suggests the tremor signal is coherent at frequencies as high as 16 Hz, and that the spatial distribution of high- and low-frequency tremor radiators is sometimes complementary.

Plain Language Summary

Tectonic tremor is a class of seismic signals whose temporal and spectral properties are distinct from the ones associated with regular earthquakes. Tremor is generally observed along fault portions located below the seismogenic zone, and is thought to be the seismic manifestation of episodic slow slip events (SSE). Elucidating the factors controlling the tremorgenic behavior of faults is important for understanding the physics of earthquakes. To study tremor along the Parkfield-Cholame section of the San Andreas Fault, we deployed three dense near-fault seismic arrays in 2018. During the first days of August 2018, the arrays recorded a strong deep transient that nucleated near Cholame and propagated toward the northwest. We analyze near-fault surface and borehole seismic data and obtain precise tremor locations. We find that tremor migrates along the fault's strike and depth at speeds that vary by about three orders of magnitude, from 5 km/day to up to 150 m/s. Rapid propagation associated with aseismic slip rates that are about 10 times faster than the tectonic rate occurs in the direction parallel to the SSE propagation, as well as backwards into previously ruptured sections. Together, these observations shed light on the complex behavior of deep fault sections.

1. Introduction

Slow slip events (SSEs) are a type of transient deformation that typically occur at slip speeds that are 1–2 orders of magnitude larger than the plate velocity (Bürgmann, 2018). SSEs are widespread, occurring on subduction megathrusts and transform faults worldwide. Because SSEs are slow they do not radiate seismic energy, and hence are not accompanied by recorded body and surface wave arrivals characteristic of typical intermediate to large magnitude earthquakes. However, they do often generate a low-amplitude seismic signal that most clearly manifests at frequencies between 1 and 10 Hz known as tectonic tremor (Obara, 2002; Wech & Creager, 2008). Tremor seismograms are characterized by emergent onsets with duration of up to several hundred seconds, which are often observed to contain sequences of similar waveform repetitions. Stacking similar repetitions obtained via autocorrelation analysis of a given tremor time-series produces waveforms that exhibit clear *P*- and *S*-wave arrivals, but are depleted in high-frequency energy relative to regular earthquakes of similar size, and are hence termed Low Frequency Earthquakes (LFEs;

Shelly et al., 2007). Methods to detect tremor usually rely on the coherency of waveform envelopes between a set of regional stations (Obara, 2002; Wech & Creager, 2008). LFE detection methods rely on extracting templates from stacked narrow band waveforms containing tremor signals, and then correlating these templates against continuous seismic data (Bostock et al., 2012; Gibbons & Ringdal, 2006; Shelly, 2017; Thomas & Bostock, 2015). The duration of the LFE template and individual tremor episodes are often of the order of 10 and a few hundreds of seconds, respectively.

Since their discovery in Japan in 2002 (Obara, 2002), tremors and associated SSEs have been the target of numerous investigations (see Beroza & Ide, 2011; Bürgmann, 2018; Peng & Gomberg, 2010, for reviews). Among the most intriguing features of tremor in subduction zones is that it exhibits a large range of propagation styles relative to the rupture speed and direction of the main SSE front. In Cascadia and Japan, deep tremor migrates together with slip along the fault's strike at speeds of up to several km per day over distances of tens of kilometers (e.g., Bartlow et al., 2011; Ito et al., 2007; Wech et al., 2009). The slow migration is often punctuated by tremor bursts propagating in the SSE slip-parallel or slip-normal direction. Those bursts are associated with secondary fronts imaged seismically, and may be roughly classified according to their propagation direction relative to the SSE front. Rapid Tremor Migration (RTM) is identified with tremor propagating in the SSE slip-parallel direction at speeds that are up to three orders of magnitude faster than the SSE rupture speed (Bletery et al., 2017; Ghosh et al., 2010; Peng & Rubin, 2016). Rapid Tremor Reversal (RTR) is identified with tremor propagating backwards into the area ruptured by the SSE at speeds of up to two orders of magnitude higher than the SSE rupture speed (Houston et al., 2011; Obara et al., 2012; Rubin & Armbruster, 2013). Elucidating the physics that gives rise to such rich behavior poses a major challenge for numerical simulations of tremor and SSEs (e.g.,Hawthorne & Rubin, 2013a; Luo & Ampuero, 2018; Rubin, 2011), and is essential for improving our understanding of the tremor source.

A widely accepted hypothesis suggests the tremor signal is made up of swarms of repeating LFEs (Shelly et al., 2007). However, testing this hypothesis is difficult because in many locations it is difficult to identify individual LFEs within tremor (Thomas & Bostock, 2015), and in places where there are catalogs of both LFEs and tremor, identified LFEs generally represent only a small fraction of the tremor signal (Guilhem & Nadeau, 2012). For example, along the Cholame segment of the SAF, only 15% of the LFEs occur within strong tremor observed regionally (H. Zhang et al., 2010). Additionally, Parkfield LFEs are predominantly located on the fault (Shelly, 2015), while some of the tremor apparently occurs off-fault (Guo et al., 2017). The relationship between tremor and LFEs is also obscured by the multitude of techniques that have been developed to detect tremor and LFEs, many of which depend on parameters, such as threshold duration, amplitudes, cross correlation coefficients or a minimum number of stations recording the LFE (Frank & Shapiro, 2014; Rubin & Armbruster, 2013; Savard & Bostock, 2015; Shelly et al., 2006; Wech & Creager, 2008). And finally, LFE templates are fundamentally narrow-band signals, which, when stacked, may resemble random impulsive arrivals. Ide (2019) addressed this issue by analyzing seismograms over a range of frequencies below the LFEs corner frequency, suggesting that signals in the 0.1–10 Hz range accompanying slow fault slip represent a continuous broadband process. However, the spatial relationship between locations of low- and high-frequency radiation during slow ruptures, and thus the relation between the seismically active and aseismically slipping fault portions, are not well constrained (Kaneko et al., 2018). The spectra of high-amplitude bursts within tremor in Cholame also appears to be more broadband than the spectra of LFEs (Fletcher & Baker, 2010). This suggests that concomitantly analyzing signals at frequencies outside the LFE corner frequency may also help resolve the broadband nature of tremor in Parkfield.

In order to determine the relationship between episodic tremor and LFEs, and to characterize frequency-dependent tremor migration patterns, we installed three dense (intersensor spacing smaller than 100 m) seismic arrays near Parkfield and Cholame, California along the central section of the San Andreas fault (Figure 1). Each array contains 25–30 three-component, short period, nodal-type sensors recording continuously at a rate of 250 samples-per-second (sps). The arrays were operative for a period of 3 months, during which they recorded a strong transient that produced high amplitude tremors. The spatio-temporal distribution of LFEs (D. Shelly, pers. comm., 2021) suggests the transient in early August was associated with a deep slow-slip event which ruptured portions of the Cholame and Parkfield sections of the SAF (Figure 2). In this paper, we employ array analysis to detect and locate tremors during the August 2018 transient. The analysis reveals tremor migration along the fault-strike and depth, tracking a deep SSE over an extended portion

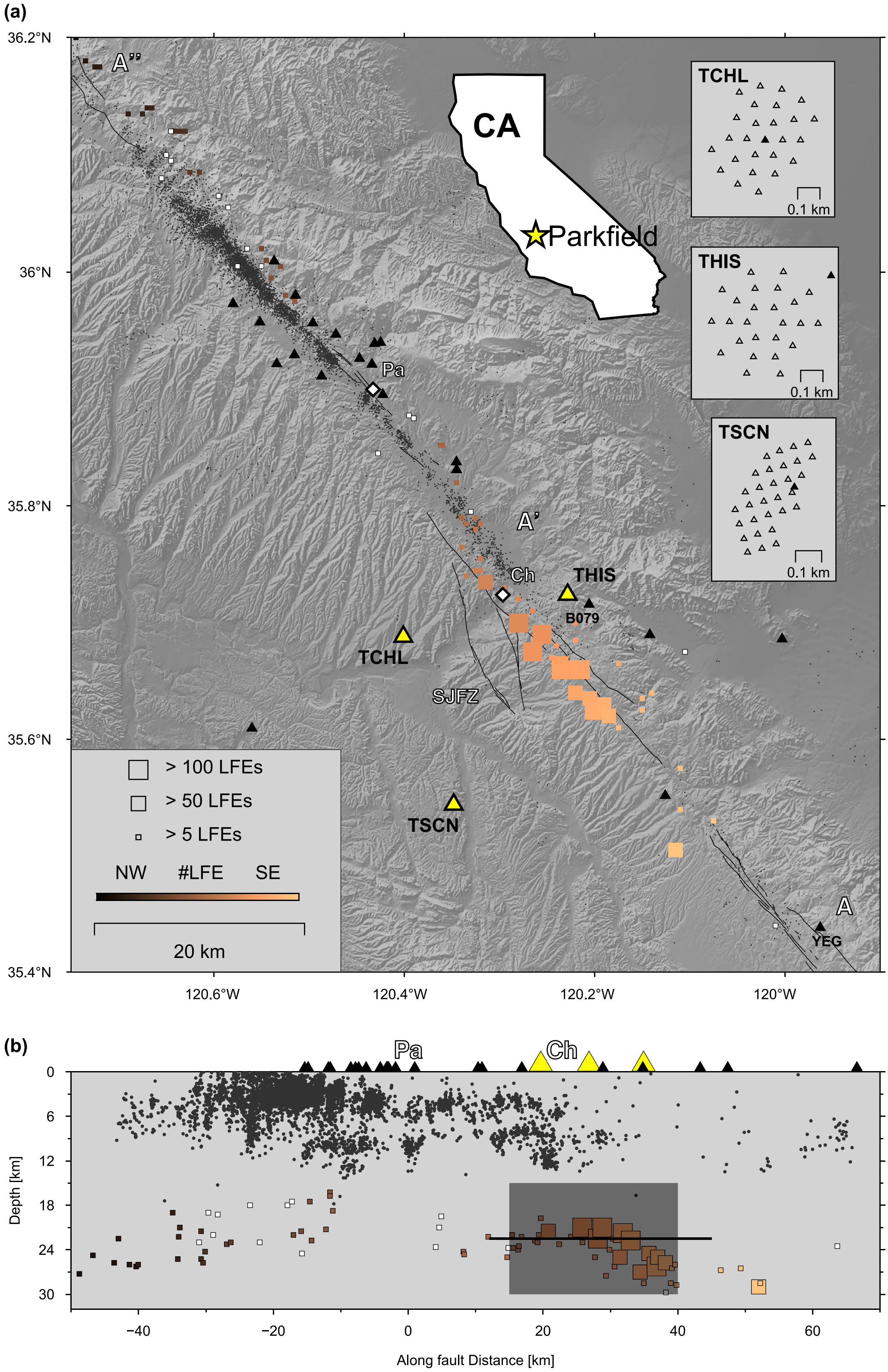
(a)
36.2°N
36°N
35.8°N
35.6°N
35.4°N
120.6°W
120.4°W
120.2°W
120°W
A”
A’
A
CA
Parkfield
Pa
Ch
THIS
B079
TCHL
SJFZ
TSCN
YEG
TCHL
0.1 km
THIS
0.1 km
TSCN
0.1 km
> 100 LFEs
> 50 LFEs
> 5 LFEs
NW
#LFE
SE
20 km
(b)
Pa
Ch
Depth [km]
0
6
12
18
24
30
−40
−20
0
20
40
60
Along fault Distance [km]

Figure 1.

of the Cholame section toward Parkfield. To better constrain the tremor depth and short-term temporal behavior, and to analyze high-frequency (>10 Hz) tremor energy, we utilize borehole data to study tremor signals during the 2018 transient. The borehole stations provide good azimuthal coverage and superb SNR conditions, and are therefore useful for obtaining high-resolution images of tremor delineating the SSE front. We continuously back-project the array and borehole data to resolve tremor migration occurring over time scales that range between 10 and 10^4 seconds, at speeds that vary over three orders of magnitude. We compare the tremor activity to LFE occurrences during the episode, and find that tremor and LFEs show a similar pattern of slow, days-long along-strike migration, but appear to differ in their short-term properties.

The remainder of this manuscript is organized as follows: In Section 2.1, we present the Cholame seismic array and borehole data set and the processing scheme. In Section 2.2, we derive empirical corrections to the array slowness measurements from local earthquake signals. We present the array analysis of the August 2018 transient in Section 3.1, and the high-resolution locations derived from the borehole data set in Section 3.2. We then analyze short-term Cholame RTMs in Section 3.3. The tremor migration style is discussed in Section 4.1, the implications for the physics of the tremor source in Section 4.2, the comparison to the LFE catalog in Section 4.3, and the frequency-dependent radiation in Section 4.4.

2. The Cholame Dense Arrays and Borehole Station Datasets

The goal of this work was to densely instrument the Cholame section of the SAF in order to capture episodic tremor accompanying an SSE. To this end, we deployed 80 nodal seismometers organized into three arrays near Cholame for a 3-month period from August to November of 2018. Nodal seismometers are easily deployable, low-cost, short-period sensors developed for oil and gas exploration (Karplus & Schmandt, 2018). While these instruments are designed for temporary deployments, previous work has shown that when densely deployed they are capable of detecting deep, small-magnitude earthquakes (Inbal et al., 2015, 2016).

The Cholame section of the SAF is an ideal scientific target for studies of slow-slip and tremor for a number of reasons. First, this region represents a transition from the creeping section of the SAF to the locked Ft. Tejon section in the shallow portion of the fault, whereas the deep fault hosts slow slip and abundant tremor activity (Figure 1). This provides an opportunity to understand the interaction between these three environments and the varying anatomy of the SAF. Second, the deployment location was very near some of the largest-amplitude LFE families identified by the regional network (Shelly, 2017), ensuring a high SNR for the temporary network. Third, each array of the temporary deployment was colocated with a Tremorscope surface station operated by the University of California, Berkeley. The network also contains borehole stations (black triangles in Figure 1) of Tremorscope, the High-Resolution Seismic Network (HRSN) and the Plate Boundary Observatory (PBO) network, which have much higher SNR than surface stations and were used, along with the surface deployments, to detect LFEs and tremors. Fourth, this section of the SAF contains LFE families that behave both episodically (as inferred from LFE activity) and continuously. The episodic families are thought to occur in response to semi-periodic slow slip events whereas the more continuous families reflect deep fault creep that occurs at an approximately constant rate (Thomas et al., 2018), hence this particular location offers the opportunity to study both deformation styles. Additionally, this deployment took advantage of the frequent occurrence of slow earthquakes in the region (as inferred from LFE occurrence patterns) improving the chances of detecting a slow earthquake during the deployment period. The deployment layout is shown in the insets of Figure 1. The three arrays were located near permanent stations TSCN, THIS, and TCHL and contained 30, 25, and 25 sensors, respectively.

Figure 1. Map and depth cross-section of the Parkfield and Cholame segments. Dots and squares are for relocated seismicity (Thurber et al., 2006) and Low Frequency Earthquakes (LFEs) (Shelly, 2017), respectively. Color of squares indicates along SAF distance relative to Parkfield, and their size indicates the number of LFEs detected between August 5 and 9, 2018. White squares are for previously detected LFEs from Shelly (2017)'s catalog, which were not active during the 2018 transient. Solid black line in bottom panel indicates the lateral extent ruptured by a slow slip event (SSE) between August 5 and 9, 2018. Gray rectangle indicates the approximate area ruptured during the Rapid Tremor Migration (RTM) on August 6, 2018 (see also Figure 9). Black and yellow triangles are for the permanent borehole and nodal array, respectively. The arrays' layout is shown in the gray rectangles, with temporary and permanent stations indicated by gray and black triangles, respectively. White diamonds indicate the location of the town of Parkfield and Cholame. Faults are indicated by black curves. Letters and abbreviations: Pa: Parkfield; Ch: Cholame; SJFZ: San Juan Fault Zone; A-A': Cholame section; A'-A": Parkfield section.

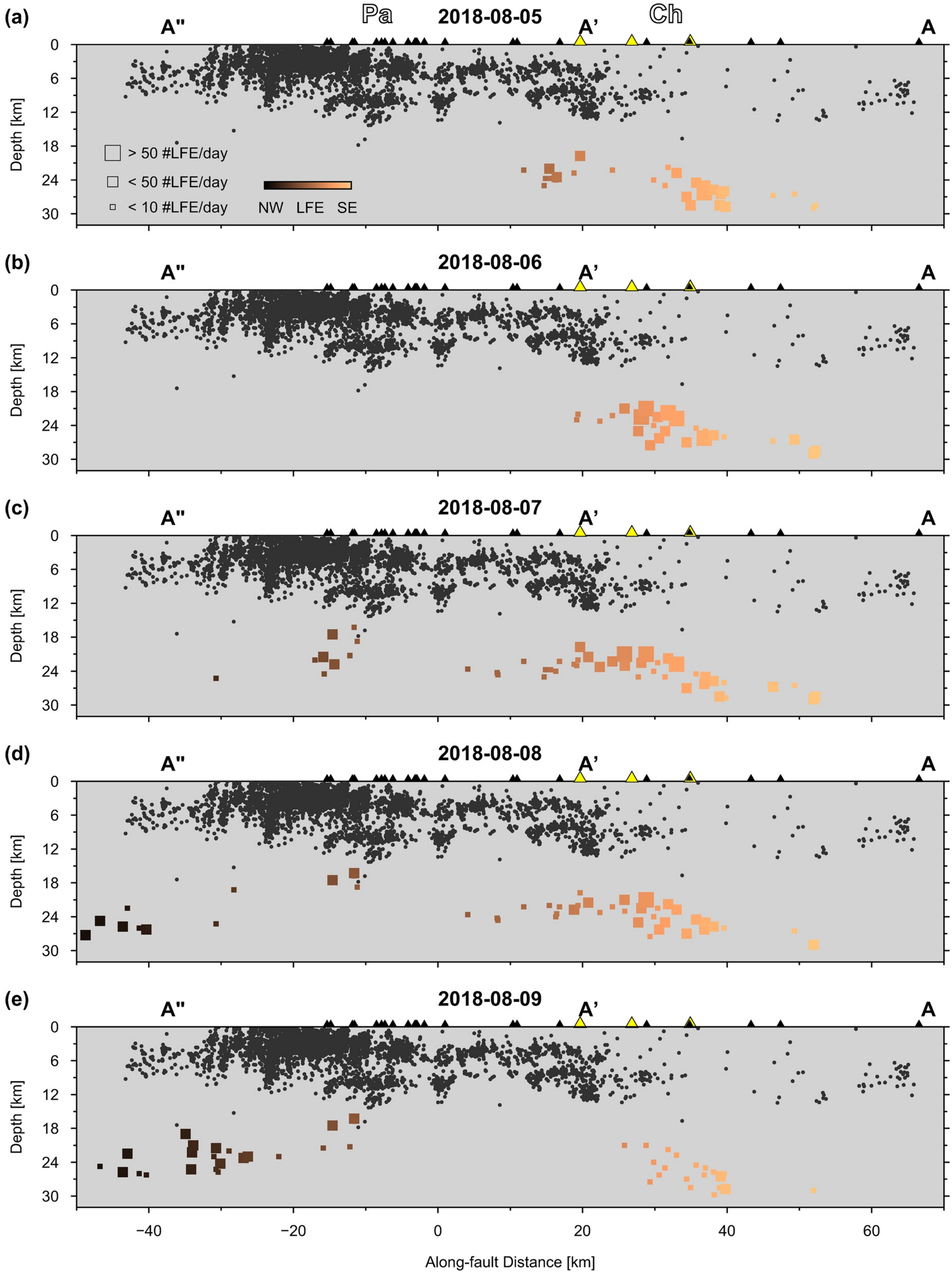

Figure 2. Spatio-temporal evolution of Low Frequency Earthquakes (LFEs) during the August 2018 slow slip event (SSE). Symbols and colors are as in Figure 1.

2.1. The Data and Processing Scheme

We utilize array analysis to resolve the slowness associated with wavefronts impinging on the array. According to theory, the intersensor coherency is maximal when the array traces are aligned with respect to the slowness of the incoming wave. The coherency may be computed in the Fourier domain, and its magnitude can be normalized by using amplitude or phase information. Here, we compute the phase coherency, since this metric has shown to be resilient against signals with time-varying intensities, which are common in our data set (Chave et al., 1987; Hawthorne & Ampuero, 2017; Riahi & Gerstoft, 2017).

We assume the incoming wavefield is impinging on a 2-D array containing N sensors at an angle θ measured with respect with the north. The angle θ is associated with the back azimuth (BAZ) pointing from the receiver toward the direction of the source. The signal recorded by the n'th sensor time-shifted relative to an arbitrary point at the center of the array may be written as:

$$x(t) = s(t - \boldsymbol{u} \cdot \boldsymbol{r_n}), \tag{1}$$

where $\boldsymbol{u} = 1/v_0(\sin\theta, \cos\theta)$ is the horizontal slowness vector, v_0 being the medium velocity, and $\boldsymbol{r_n}$ is a vector pointing toward the center of the array. Applying the Fourier transform to Equation 1 gives:

$$X(\omega) = S(\omega)e^{-i\omega(\boldsymbol{u}\cdot\boldsymbol{r_n})}, \tag{2}$$

where ω is the angular frequency. The phase coherency between each pair of array sensors averaged over M frequency bands is:

$$C_{ij} = \mathrm{Re}\left[\frac{1}{M}\sum_{M}\frac{X_i(m)}{|X_i(m)|}\frac{X_j^*(m)}{|X_j(m)|}\right]. \tag{3}$$

For correlated signals, the product of the complex components of the vectors X_i and X_j gives $C_{ij} = 1$, and for decorrelated signals $C_{ij} = 0$. We average the coherency over all available pairs, and associate the slowness that maximizes the array-averaged coherency with the detected signal. We denote the maximum array-averaged coherency C_{max}, and use its statistical properties to define a detection criteria.

We present applications of the coherency-based analysis (Equations 1–3) using two datasets: the dense arrays and the regional borehole stations. The two datasets are complementary such that they provide insight into processes occurring over a wide range of spatial and temporal scales. The analysis of each data set differs according to the value of a dimensionless parameter R equal to the ratio between the array aperture and hypocentral distance. For the dense array data set $R \ll 1$ and we may rely on the plane-wave approximation when analyzing the seismic wavefield. In this case, the coherency C_{ij} for each seismogram pair in each time window is computed for horizontal slowness values ranging between −0.5 and 0.5 s/km separated by 0.01 s/km increments by shifting the traces according to a pre-computed time-delay table. We demean and filter the vertical-component array data between 0.5 and 10 Hz using a fourth-order Butterworth filter and then downsample the data to 125 sps. We compute the coherency for 1.5 s consecutive time horizontal slowness vector $\boldsymbol{u}$ corresponding to C_{max} according to:

$$BAZ = arctan(u_x, u_y) + \pi \text{ and } V_{app} = 1/\sqrt{u_x^2 + u_y^2}. \tag{4}$$

In the second application, we analyze tremor occurring beneath the Tremorscope, PBO, and HRSN borehole stations (Figure 1). This station configuration differs in several aspects from the dense-array configuration: First, for the borehole station configuration $R \geq 1$, and the plane-wave assumption is not valid. A corollary is that the borehole network, which extends across the Cholame and Parkfield sections (Figure 1), samples the four quadrants of the source focal sphere. Since the tremor source mechanism is unknown, we cannot correct for the signal's polarity. Additionally, the propagation paths between the tremor sources to each of the recording borehole stations are quite different, and hence result in different waveforms. We therefore resort to analyzing waveform envelopes, which exhibit a higher level of similarity. Second, we are interested in measuring the coherency of high-frequency tremor bursts whose duration is less than two seconds, which is shorter than the propagation time of signals traversing the borehole network.

To address these issues, we back-project the phase coherency between waveform envelopes onto the volume beneath the borehole stations. The method is similar to the one employed by Inbal et al. (2015) to study weak sources beneath the dense Long-Beach seismic array. However, unlike Inbal et al. (2015)'s back-projection procedure, here we back-project the array-averaged envelope phase-coherencies. To do so, we take the following steps. First, we compute the envelope of the filtered signals by squaring and smoothing using a 0.25 s running median window. Next, we low-pass filter the envelopes using a fourth-order Butterworth filter with 0.1 Hz corner frequency. Next, we obtain a crude location of the low-frequency signal by (a) shifting the envelopes according to travel-times computed for a 3-D grid of sources spaced at 1 km increments using 1-D profiles extracted from a local velocity model (Thurber et al., 2006), and (b) computing C_{max} for 30 s windows according to the scheme outlined above. Then, we shift the envelopes according to the offsets that correspond to C_{max} obtained for the low-frequency signal. This effectively cancels signal move-outs that are longer than the 2 s analysis window we employ. Finally, we bandpass filter the offset seismogram for a range of frequencies >4 Hz, envelope the signals, and compute C_{max} for each frequency range using 2 s windows with 1 s lags.

2.2. Calibration Using Local Earthquake Signals

Next, we analyze local earthquake data in order to derive empirical corrections for the observed slowness at the three arrays, and use the corrections to calibrate the observed back-azimuths during the August 2018 transient. Although the earthquake focal depths are systematically shallower than the tremor sources, we will show in Section 3.1 that the corrected back-azimuths obtained for the deep tremor signals are consistent between the three arrays. Moreover, the along-strike migration trend we resolve is also in agreement with LFE locations determined independently, suggesting the corrections we derive using signals due to sources located at depth <12 km are applicable to signals due to sources located at a larger depth.

In principle, the source location may be determined from the intersection of rays whose horizontal slowness is resolved by the arrays, and that are back-projected onto the source (e.g., Meng et al., 2014). However, due to complex structure, the apparent slowness may be significantly different from the true slowness. An empirical correction term applied to the observations may be obtained from the analysis of well-located events (e.g., Bondár et al., 1999; Flanagan et al., 2012). Assuming a simplified 1-D model, the amplitude of the deviation from the true back azimuth may be used to infer the geometry along the raypath (Niazi, 1966).

To calibrate the array measurements, we analyze *P*-wave arrivals from 206 earthquakes registered in the regional Northern California Earthquake Data Center catalog, which occurred within 80 km from the arrays between August and October, 2018. We apply the array analysis (Section 2.1) to a window of vertical-component data starting 2 s before the *P*-wave arrival, and record the horizontal slowness as a function of time. Figure 3 presents the results of this analysis. Panel (a) presents the recorded vertical ground motion during the passage of the *P*-wave train due to a $M_w = 1.9$ earthquake that occurred 65 km away from array TSCN. Panels (b) and (c) present C_{max}, back azimuth, and horizontal slowness time series. As expected, values of C_{max} and horizontal slowness are consistent with impulsive arrivals due to a deep tectonic source. However, the apparent back azimuth at array TSCN deviates from the true back azimuth by as much as 30°, suggesting along-path structural complexities.

The sharp increase in the coherency level during the *P*-wave arrival is also characterized by low scalar slowness values (≈0.1 s/km) relative to the preevent 2 s window containing noise. Thus both C_{max} and the scalar horizontal slowness may be used to discriminate sources of tectonic origin. The noise in the 2–8 Hz frequency band is mostly dominated by low-incident surface waves that result from anthropogenic activity (e.g., Inbal et al., 2018; Johnson et al., 2019; Riahi & Gerstoft, 2017). The decrease in the horizontal slowness during the *P*-wave arrival in panel (c) indicates that waves due to a deep source are incident on the array.

Figures 3d–3f present the difference between the true and apparent back azimuth as a function of the true back azimuth to local earthquakes whose maximum coherency level during the *P*-wave train exceeds 0.4. The dashed line is a sinusoidal fit to the observations, and the fitted function sign change is indicated by the vertical dotted line in each panel. If the deviation of the apparent back azimuth is assumed to be the result of a dipping reflector underlying the array, then the change in the sign of the deviation is indicative of the strike of the reflector (Niazi, 1966). For the three arrays, we find that the deviation from the true back azimuth may be fitted assuming a reflector striking at 240–260°, compatible with a structure striking at a high angle relative to the SAF strike. The implications of this result on our understanding of the regional structure are discussed in Appendix A.

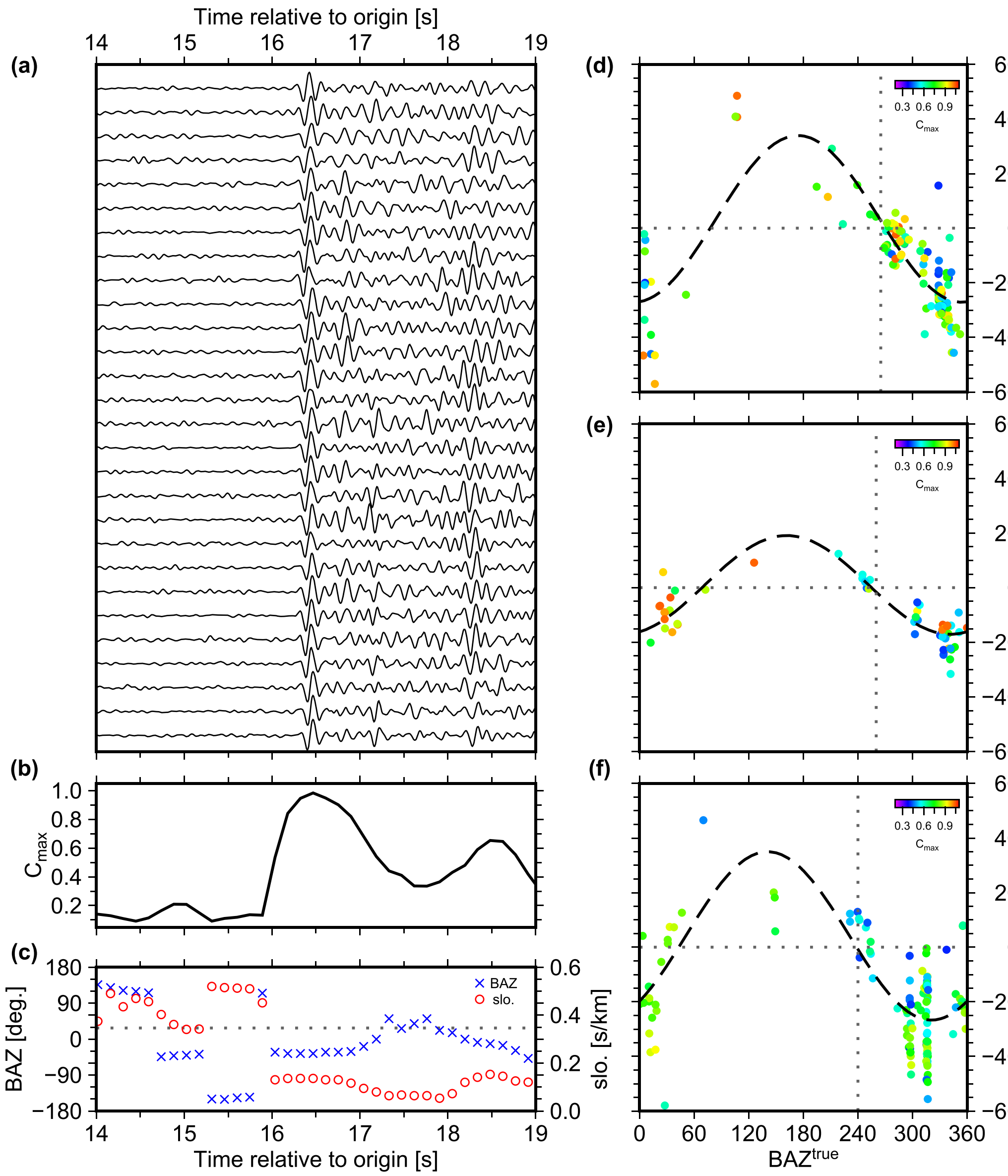

Figure 3. Analysis of Parkfield seismicity using dense arrays. (a) Vertical ground velocity recorded at array TSCN due to a $M = 1.9$ earthquake. Traces are normalized by their maximum amplitude. (b) Coherency as a function of time. (c) Back azimuth and horizontal slowness as a function of time. Red circles and blue crosses are for back azimuth and slowness measurements, respectively. Dotted line indicates the back azimuth to the catalog location. (d–f) The difference between the apparent and true back azimuth as a function of the true back azimuth to local earthquakes. Each circle is for a different earthquake. Dashed line is a sinusoidal fit to the data. Vertical dashed lines indicate the true back azimuth corresponding to the sign change of the fitted sinusoid, and horizontal dashed lines the zero crossing. Circles are colored according to C_{max}. (d) Array TSCN. (e) Array THIS. (f) Array TCHL.

Following this analysis, the epicentral locations of sources along the SAF may be determined from the intersection of rays pointing in the direction of the back azimuth resolved at each of the arrays. Determining the source depth requires that we also correct for the potential bias in apparent incidence angle using a detailed velocity model. However, only a short segment of the fault near Cholame is azimuthally well covered such that the array-resolved hypocentral locations of sources lying along much of its length are well constrained. We therefore use the corrected back azimuth measurements to resolve along-strike tremor migration during the August 2018 transient, and do not attempt to constrain the tremor depth based on the dense array recordings. Instead, we utilize the borehole data to determine the hypocentral location for sources lying along the Cholame and Parkfield segments.

3. Results

In order to shed light on the behavior of deep SAF tremors, we apply our back-projection method to image seismic radiation during the SSE that ruptured the Cholame and Parkfield sections during the first days of August 2018. Next, we present a detailed space-time analysis of tremor episodes and LFEs on timescales ranging between 10 and 10^4 seconds, and highlight salient features of tremor in Cholame. We begin by presenting the results of the array data analysis, and then compare the locations of 100-s-long bursts analyzed by using the array and borehole data.

3.1. Space-Time Analysis of SAF Tremor Resolved via a Multiarray Approach

We focus on a 9-day interval beginning on August 3, 2018, and apply the analysis described in Section 2.1 to continuous data recorded by the arrays over this time period in order to track the slowness, array-averaged coherency, and tremor rates and locations as a function of time. We compare these locations to the LFE catalog locations (D. Shelly, pers. comm., 2021; the catalog is available in the Supplementary Materials section). To discriminate time windows containing tremor we apply a coherency and slowness criteria: signals with $C_{max} > 0.25$ and $|\boldsymbol{u}| < 0.3$ s/km (i.e., $V_{app} > 3.3$ km/s) are automatically associated with a deep tectonic source. These detections are subjected to the additional requirement that the back azimuth measurements are consistent between the arrays. This means that the resolved back-azimuths from each array must intersect within a maximum distance from the fault. Note that for each source-array pair, there exists a range of acceptable slowness values whose distribution is a function of the SNR and array geometry. The range of back azimuth extending from the array toward the source forms a circular sector whose radius is measured from the array, and which bounds the acceptable epicentral source locations. The multiarray-based epicentral location may be obtained from the intersections of these sections (see for example the maps in Figures 5e and 5f). Since the polygons formed from back azimuth intersections from more than two arrays sometimes do not overlap, we select the polygon located closest to the fault as the most probable source epicentral location. The error on the back azimuth and scalar slowness are derived from bootstrapping applied to the array data set (see Supporting Information S1). Using these tests, we find that for detections with $C_{max} \sim 0.2$, the back azimuth errors are $12°, 15°$, and $18°$ for arrays TSCN, TCHL, and THIS, respectively, and the horizontal slowness errors are 0.03 s/km, 0.04 s/km, and 0.04 s/km for arrays TSCN, TCHL, and THIS, respectively.

We find that for 0.04% of the analyzed windows, both coherency and slowness exceed our criteria, and are associated with back azimuth measurements (and respective errors) that intersect on polygons whose centers lie less than 10 km from the SAF surface trace. To the best of our knowledge, the area does not include anthropogenic sources such as train rails, wind-farms, and major highways, which were identified by Inbal et al. (2018) as producing signals in the tremor bandwidth that may confuse array-based techniques as the one implemented here. Nor do we expect signals due to oil pumping in the Lost Hills oilfield, agricultural water pumping, or air traffic (Meng & Ben-Zion, 2018), to map onto deep focal locations or exhibit the characteristics of the tremor we observe. Additionally, using the coherency criteria ensures the robustness of the resolved slowness during high-coherency windows.

Figure 4 presents a summary of the array analysis results. Panels (a–c) show a time series of the back azimuths resolved by the three arrays matching our detection criteria. We find two main tremor-producing sources, to the north and to the south of the town of Cholame (back azimuth of 140–150° and 290 to 330° relative to array THIS). The tremor activity is characterized by short (up to several minute long) bursts of coherent signals that are well observed by arrays THIS and TSCN, where the SNR level is generally higher than in array TCHL. These durations are comparable with the ones resolved by Ryberg et al. (2010) and Fletcher and Baker (2010), who also used array analysis to detect SAF tremors. A more detailed comparison with these studies is presented in Section 4.4.

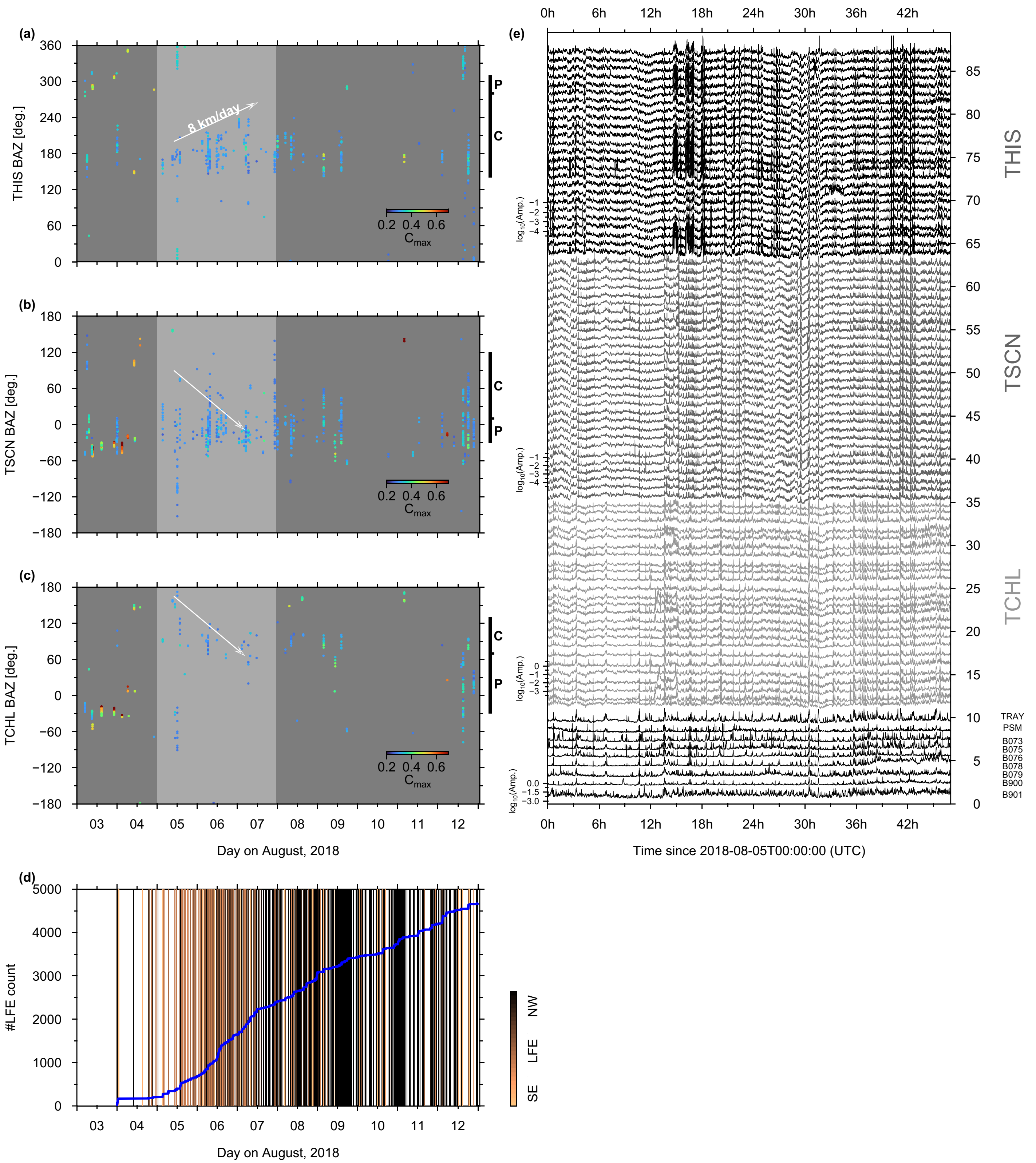
(a)
THIS BAZ [deg.]
360
300
240
180
120
60
0
8 km/day
P
C
0.2 0.4 0.6
C_{max}
(b)
TSCN BAZ [deg.]
180
120
60
0
−60
−120
−180
C
P
(c)
TCHL BAZ [deg.]
C
P
03
04
05
06
07
08
09
10
11
12
Day on August, 2018
(d)
#LFE count
5000
4000
3000
2000
1000
0
NW
LFE
SE
(e)
0h
6h
12h
18h
24h
30h
36h
42h
Time since 2018-08-05T00:00:00 (UTC)
$\log_{10}$(Amp.)
−1
−2
−3
−4
0
−1.5
−3.0
85
80
75
70
65
60
55
50
45
40
35
30
25
20
15
10
5
0
THIS
TSCN
TCHL
TRAY
PSM
B073
B075
B076
B078
B079
B900
B901

Figure 4.

Beginning on August 5, we identify a significant increase in the rate of detections along the Cholame section, which continues for ∼3.5 days. The 1–10 Hz vertical energy time-series (ground velocity-squared envelopes smoothed using a 60 s window) during this time is shown in Figure 4e. The tremor bursts show as arrivals with near-vertical moveout across the arrays and the regional network stations (bottom traces in Figure 4e). Note that the rate of high-frequency bursts significantly increases on August 5th, at around 12 UTC.

Most of the tremor we observe prior to August 5 is located northwest of Cholame. The increase in the rate of detections beginning on August 5 is accompanied by a shift in the locus of tremor activity from the Parkfield segment to the Cholame area. The transition from Parkfield to the Cholame section is quite abrupt. We find that C_{max} values for tremor originating from the Cholame section are generally lower than the ones associated with the Parkfield section. Yet, over the time window between August 5 and August 6 the majority (75%, 65%, and 60% of detections at arrays THIS, TCHL, and TSCN, respectively) of tremor is associated with the Cholame section rather than with the Parkfield section. Note that our detection scheme identifies the signal's location with the slowness that maximizes the array-averaged coherency, and hence is unable to discriminate between a single or multiple active sources. Thus, the apparent activation of the Cholame section may be due to a decrease of tremor amplitude along the Parkfield section, causing the Parkfield activity to be masked by the activity in Cholame. A second alternative is that the tremor rate along the Parkfield section is reduced around August 5, yet its amplitude is preserved. Presently, we cannot discriminate between these two options.

Between August 5 and 8, tremor is observed to migrate primarily along the SAF strike from south-east of Cholame toward Parkfield. The lateral extent of the slow rupture is indicated in Figure 1b. The migration can be roughly divided into two stages. In the first, tremor activity initiates south of the town of Cholame and migrates toward the intersection between the SAF and the San Juan Fault Zone (SJFZ; see Figure 1). The activity in that area peaks around August 6 and continues until August 9. The second stage occurs between August 6 and 8 and is characterized by intermittent activity from a stationary source located along the SAF-SJFZ intersection (e.g., back azimuth between −30° and 0° relative to array TSCN; Figure 4b) accompanied by a second front moving along the SAF strike toward Parkfield. This interval is well observed by arrays THIS and TSCN (Figures 4a and 4b, respectively). Note that at the scale of Figure 4, the migration resolved by array TSCN appears to show the tremor region is shrinking, and not expanding as resolved by the two other arrays. This is due to bursts of tremor that occur between 02:00:00 and 08:00:00 UTC on August 6 and that are located near the Parkfield section (i.e., −60° to -30° relative to array TSCN). Also, note that the along-strike migration toward the northwest during stage 2 is well resolved by array TCHL, yet the number of detections exceeding our criteria in this array is small. This compact along-strike distribution of locations observed at array TCHL suggest that it mostly sensitive to the propagating front, and less so to the stationary source located toward the central portion of the Cholame section. We also find that the arrivals to array TSCN from the stationary source active during stage 2 cover a range of back-azimuths between about −10°–+10°, likely reflecting the tremor distribution along the fault's strike as well as some level of error on the resolved back azimuth. The along-strike migration speeds that we infer for the front propagating during stage 2 are ∼8 km/day, in agreement with previous estimates of slow ruptures along these segments (Shelly, 2015, 2017).

Figures 5 and 6 present the array analysis of a several-minute long tremor episode that occurred on August 5. Tremor energy during this episode fluctuates, and is strongest between 150 and 300 s. This strong burst is associated with tremor that is slowly migrating along the SAF strike from Cholame toward Parkfield. The interval with maximal tremor energy is characterized by a relatively narrow range of slowness resolved by arrays THIS and TSCN (Figures 5a and 5b). Analysis of resolved back azimuth for temporally clustered

Figure 4. Dense array analysis of the August 2018 tremor and temporal evolution of low frequency earthquakes (LFEs). (a–c) Back azimuth as a function of time since August 3, 2018. Arrows indicate tremor migration direction and speed. Circles are colored according to C_{max}. Vertical bars to the right of each panel indicate the along-strike extent of the Parkfield and Cholame sections, denoted by the letters P and C, respectively (see also Figure 1a for segment boundaries). Light-gray rectangle highlights the window shown in panel (e). (a) Array THIS. (b) Array TSCN. (c) Array TCHL. (d) Cumulative LFE counts as a function of time. Vertical bars indicate LFE origin times with colors corresponding to the LFE along-strike location. Cholame and Parkfield LFEs are shown in light and dark color, respectively. (e) Log of the vertical ground velocity squared recorded by the arrays and regional stations between August 5 and 6, 2018. Starting with indices >10, light-gray, dark-gray, and black curves are for the TCHL, TSCN, and THIS arrays, respectively. Bottom 10 traces are for the regional permanent stations. Station names are indicated to the right of each trace. Vertical scales indicate the amplitude within each station subset.

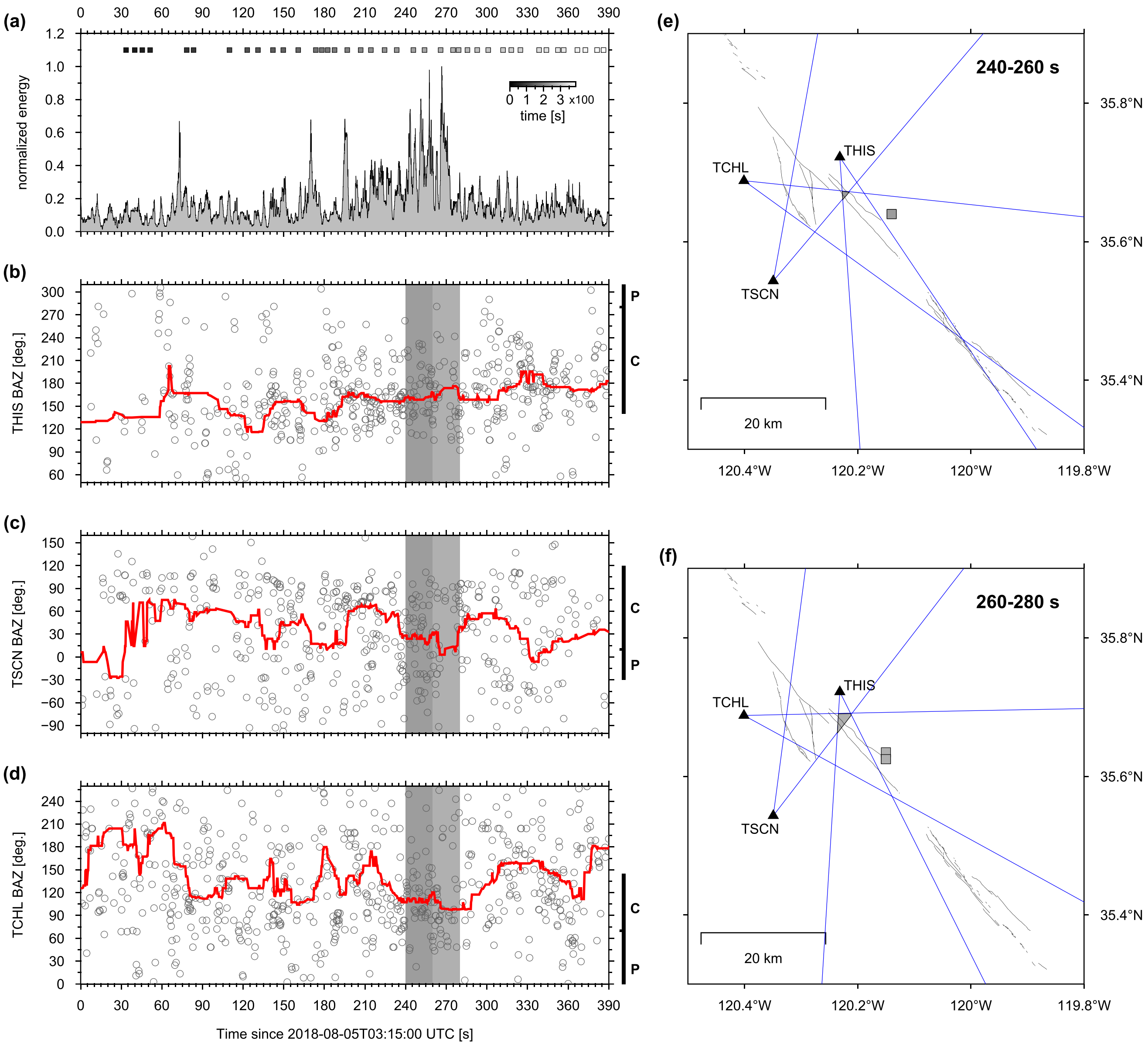

Figure 5. Dense array analysis of a tremor episode recorded on August 5, 2018. (a) Envelope of vertical ground velocity squared recorded at surface station TSCN. Low frequency earthquake (LFE) times are indicated by the squares at the top of the panel, colored in shades of gray according to the scale in panel (a) (a–c). Back azimuth as a function of time. Gray rectangles indicate two windows whose associated tremor locations are shown in panels (e and f). Gray circles are for individual detections, and red line is the median value computed for 30-s-long tremor windows. Vertical bars indicate the extent of the Parkfield and Cholame sections, denoted by the letters P and C, respectively. (a) Array THIS. (b) Array TSCN (c) Array TCHL. (e–f). Location of tremor and LFEs during two time windows between 240 and 280 s. The blue lines indicate the range of accepted back azimuth resolved at each array. The gray triangle formed by the intersecting back azimuth ranges indicates the tremor epicentral location estimates. The black triangles indicate the location of the arrays. The squares indicate the location of LFEs active between 240 and 280 s, colored in shades of gray according to the scale in panel (a). (e) Locations for the interval between 240 and 260 s (f) Locations for the interval between 260 and 280 s.

tremor detections locates the source along the northern portion of Cholame near the Cholame-Parkfield intersection (Figure 5e).

The apparent velocity resolved for this episode is shown in Figure 6. During the strongest tremor bursts, the apparent velocity is associated with values that are significantly higher than the background levels, indicating the wavefield is dominated by energy emitted from a deep tectonic source. We also observe an increase in apparent velocity correlated with the peak in tremor energy, between about 240 and 280 s. Since the back azimuth measurements indicate tremor is propagating slowly along the fault's strike (e.g., Figures 5e and 5f),

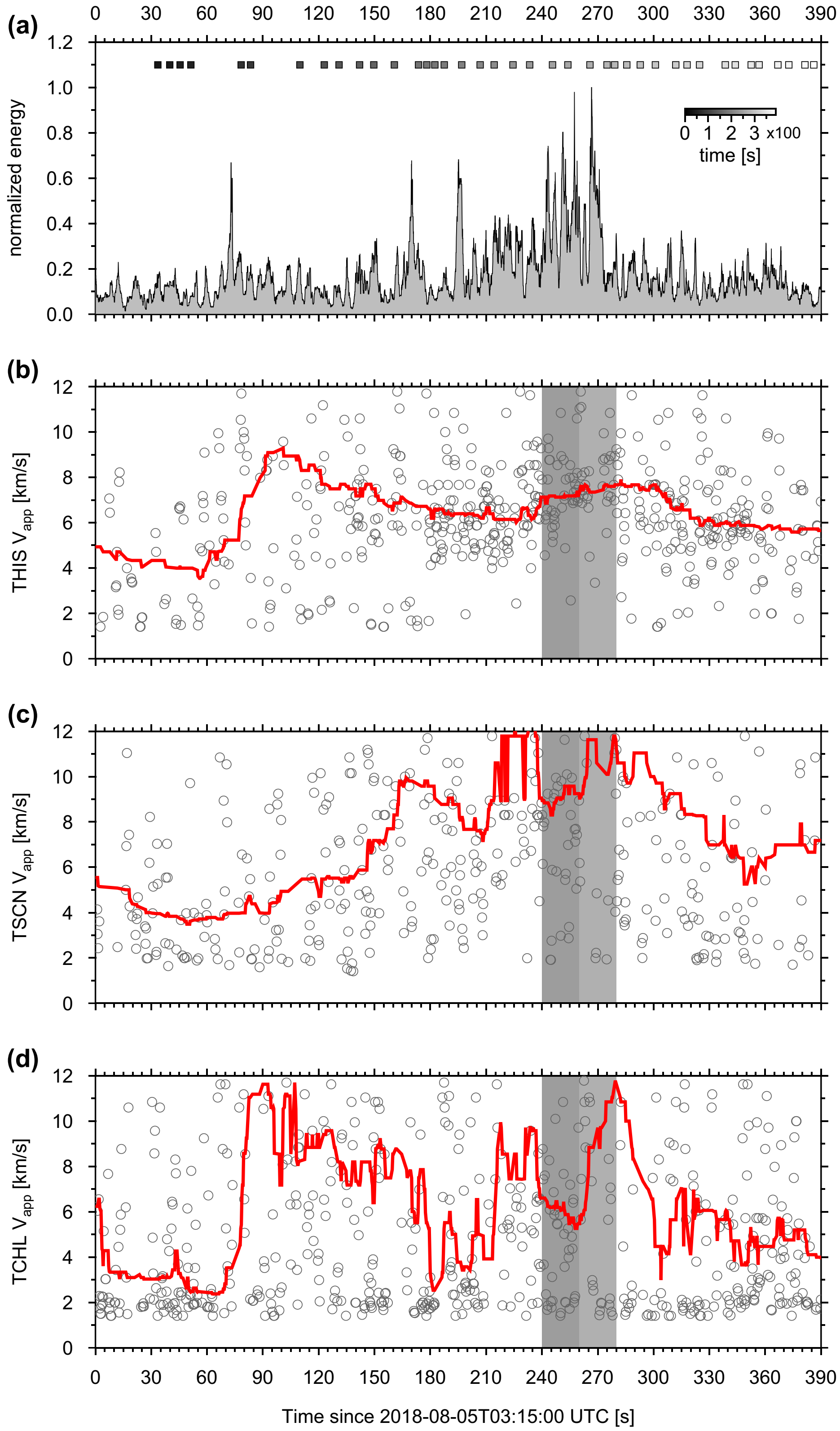

Figure 6. Apparent velocity as a function of time during the August 5, 2018 tremor episode. Symbols are as in Figure 5.

the increase in apparent velocity suggests the tremor source depth is increasing. During this interval, the apparent velocity is observed to increase at all three arrays (between 250 and 270 s Figures 6b–6d), however the degree of increase is different at each of the arrays, and is largest at the off-fault arrays. This phenomenon is the result of the source-array geometry. Since the raypath to arrays located off the fault is more sensitive to the source depth than the path to near-fault arrays, we expect the source depth increase to have a strong effect on the apparent velocity observed at arrays TSCN and TCHL, which are located as much as 20 km away from the fault, but only a small effect on the values resolved by the near-fault array THIS. Our observations confirm this hypothesis: the apparent velocity increase is only modest at array THIS (Figure 6b), but is much more dramatic at arrays TSCN and TCHL (Figures 6c and 6d, respectively). We further analyze the evolution of tremor depth during the August 5 episode using the borehole data in Section 3.2.

The 2018 SSE we identify is accompanied by strong LFE activity (D. Shelly, pers. comm., 2021; see Shelly, 2017 for the LFE catalog compilation method, and supplementary materials for the LFE catalog analyzed here). The spatio-temporal evolution of LFE activity during the August 2018 transient is shown in Figure 2. LFE rates significantly increase on August 5, with many events occurring in families located almost directly beneath the arrays between August 6 and August 8. This stage is characterized by migration of LFE activity. LFE rates are observed to gradually increase from Cholame toward the intersection between the Cholame and Parkfield sections and further to the northwest (Figures 2b–2d). The short episode of tremor shown in Figures 5 and 6 also contains a number of LFEs, whose times are indicated by the squares in the top panels in each Figure. The LFE epicenters are indicated by the squares in Figures 5e and 5f, and are found to lie near the tremor locations resolved by the arrays. However, the extent of along-depth propagation derived from the LFE catalog is somewhat smaller than the extent we infer based on the analysis of the borehole data, as is further discussed in Section 3.2.

Thus, the array analysis suggests that tremor migration is roughly consistent with LFE activity, however the sparse LFE-family locations make the along-strike and depth extent of LFE migration more difficult to resolve. Since most of the LFE activity between August 8 and 9 occurs along the Parkfield section (section A’-A” in Figures 2d and 2e), in an area that is not well covered by the arrays, the number of array-detected tremors on these days is small.

3.2. Tremor Locations From Phase Coherency Back-Projection Applied to Regional Borehole Data

The borehole station distribution provides azimuthal source coverage that far exceeds the nodal arrays coverage. Moreover, the borehole recording conditions provide superb SNR levels relative to the surface sites, allowing us to probe the tremor signal at frequencies higher than 10 Hz. We locate tremor signals by computing C_{max} for waveform envelopes recorded by the borehole stations. We augment the borehole array with surface site YEG located near the southern terminus of the Cholame section. We select 102 5-min windows of vertical component data containing tremors occurring between August 5 and August 9, 2018. The analysis scheme is detailed in Section 2.1.

Figure 7 presents the analysis of borehole data containing a strong episode of tremor observed on August 5, which was discussed in Section 3.1, and shown in Figures 5 and 6. This strong burst is one of several tens of several-minute-long tremor episodes recorded during the 2018 transient, which are located near the Cholame-Parkfield intersection, and which give rise to tremor amplitudes that increase well above the noise level at borehole stations located up to 50 km away from the epicenter. We find that the locations we derive from the wide-aperture borehole network are consistent with results we obtained from the temporary dense arrays, which indicated the tremor source is mainly propagating along-depth (Figure 6). This is confirmed by the results in Figure 7b, which presents the median tremor depth and the value of C_{max} computed for 15-s-long windows. The spatiotemporal evolution resolved by the borehole data indicates the tremor depth is increasing from 20 to about 32 km, starting at about 180 s, and lasting for 120 s during which the strongest and most coherent tremor is observed. Note that LFE activity during the August 5 episode, which is indicated by the squares in Figures 7b, is distributed over a narrower depth range. However, the deepening trend observed for the strongest and most coherent tremor is consistent with deepening of the LFEs from about 26–29 km during this time window. Also, note that the tremor depth errors are about 5 km for the most coherent sources (i.e., $C_{max} > 0.5$; see Supporting Information S1 and Figure 9d). Thus,

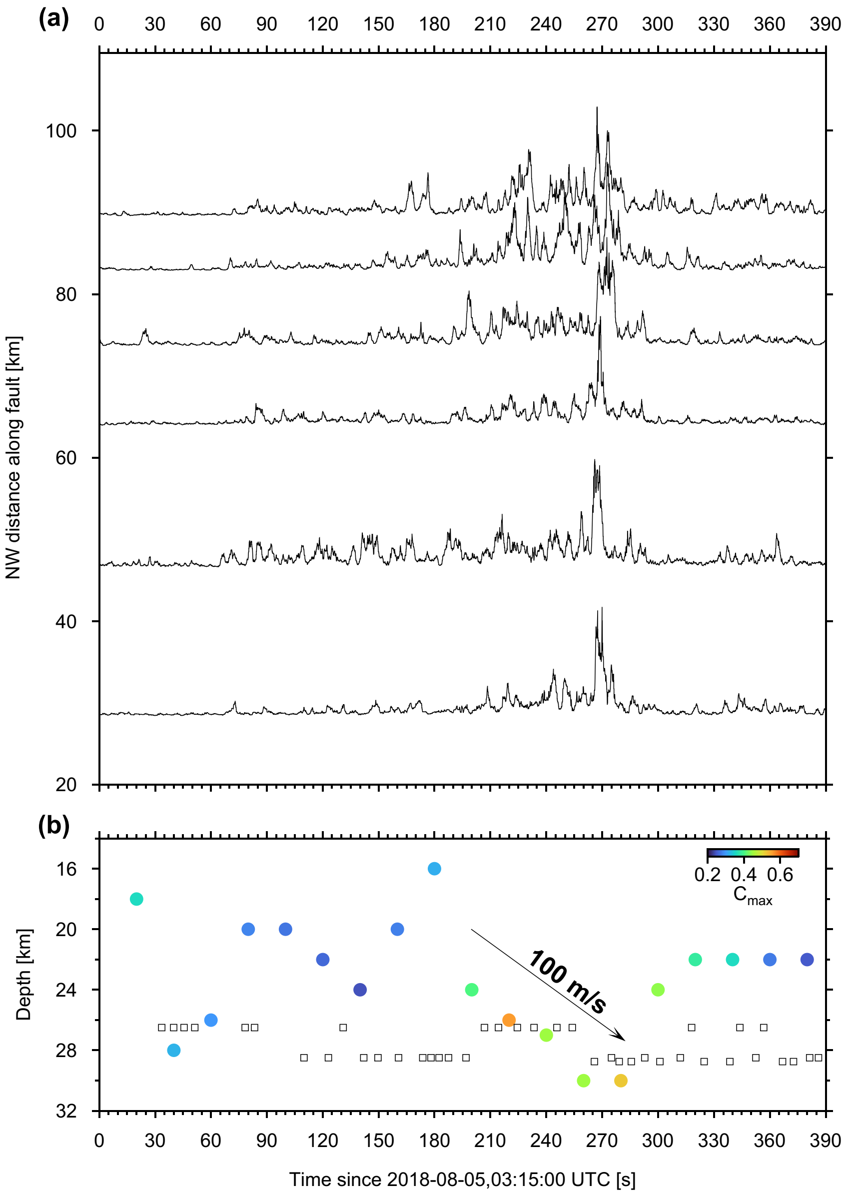

Figure 7. Tremor locations during the August 5, 2018 tremor episode obtained from analysis of the Parkfield and Cholame permanent borehole stations. (a) Envelopes of ground velocity squared containing episodic tremor from August 5, 2018. Stations are sorted according to their distance along the fault's strike from southeast to northwest, and are indicated by blue triangles in Figures 8c and 8d. (b) Median tremor depth computed for 40-s-long windows, and low frequency earthquake (LFE) depths as a function of time. The color indicates the value of C_{max} for each window, and the squares indicate the depth of LFEs.

the depth separation between tremor and LFEs between 200 and 300 s is likely smaller than the combined uncertainties on the locations of the two sources. Weaker tremor occurring between 60 and 200 s is about 8 km shallower than the LFEs occurring during the same time period, however this less coherent tremor is not as well located. The average along-depth migration we infer for the tremor burst occurring between 180 and 300 s is about 100 m/s, which is high compared to migration velocities of up to 25 m/s inferred form LFE rates (Shelly, 2015).

Figures 8a and 8b present an example of a tremor burst analyzed using the borehole data. The top row presents horizontal ground velocity envelopes, which contain tremor energy recorded during a 4-min-interval on 6 August 2018 along the SAF strike. Panel (a) shows data filtered between 4 and 8 Hz, and panel (b)

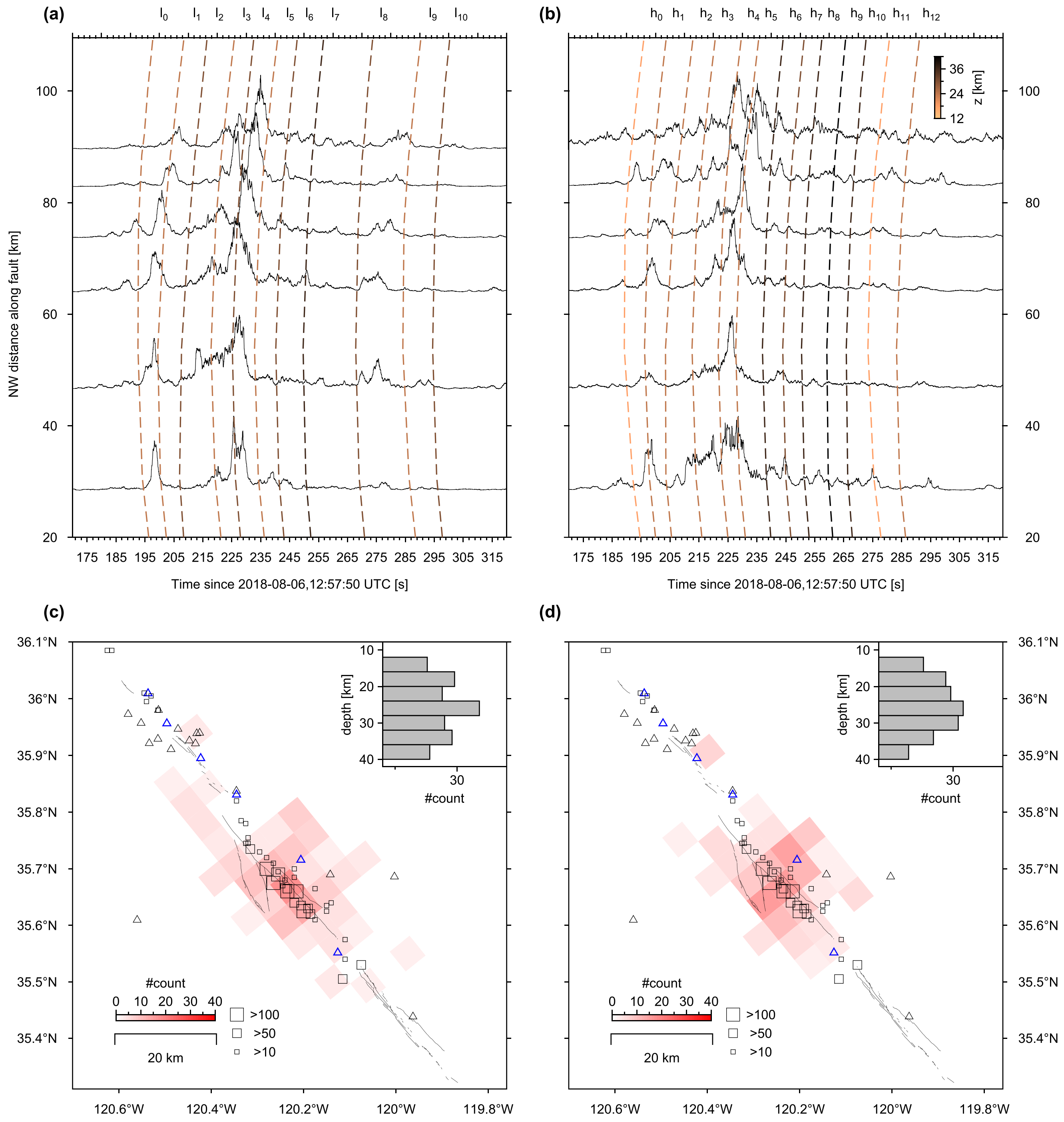

Figure 8. Tremor locations obtained from analysis of the Parkfield and Cholame permanent borehole stations. (a and b) Envelopes of ground velocity squared containing representative episodic tremor from August 6, 2018. Stations are sorted according to their distance along the fault's strike from southeast to northwest, and are indicated by blue triangles in panels (c and d). Amplitudes are normalized by their maximum amplitude. Dashed curves indicate the travel-time moveout for locations obtained in this study. Letters above each panel denote individual detections, with and *h* indicating detections in the 4–8 and the 8–16 Hz, respectively, and color indicating the associated hypocentral depth estimates. (c and d) Tremor and LFE density for the interval between August 5 and 9, 2020. Tremor densities are shown by shades of red. The permanent stations are shown by triangles. low frequency earthquake (LFE) locations (for families occurring beneath the circumference of the area covered by the borehole stations) are indicated by the squares, with the size of each square indicating the LFE count. Subpanels show the tremor depth distribution. (a, c). Analysis of the 4–8 Hz frequency range. (b, d) Analysis of the 8–16 Hz frequency range.

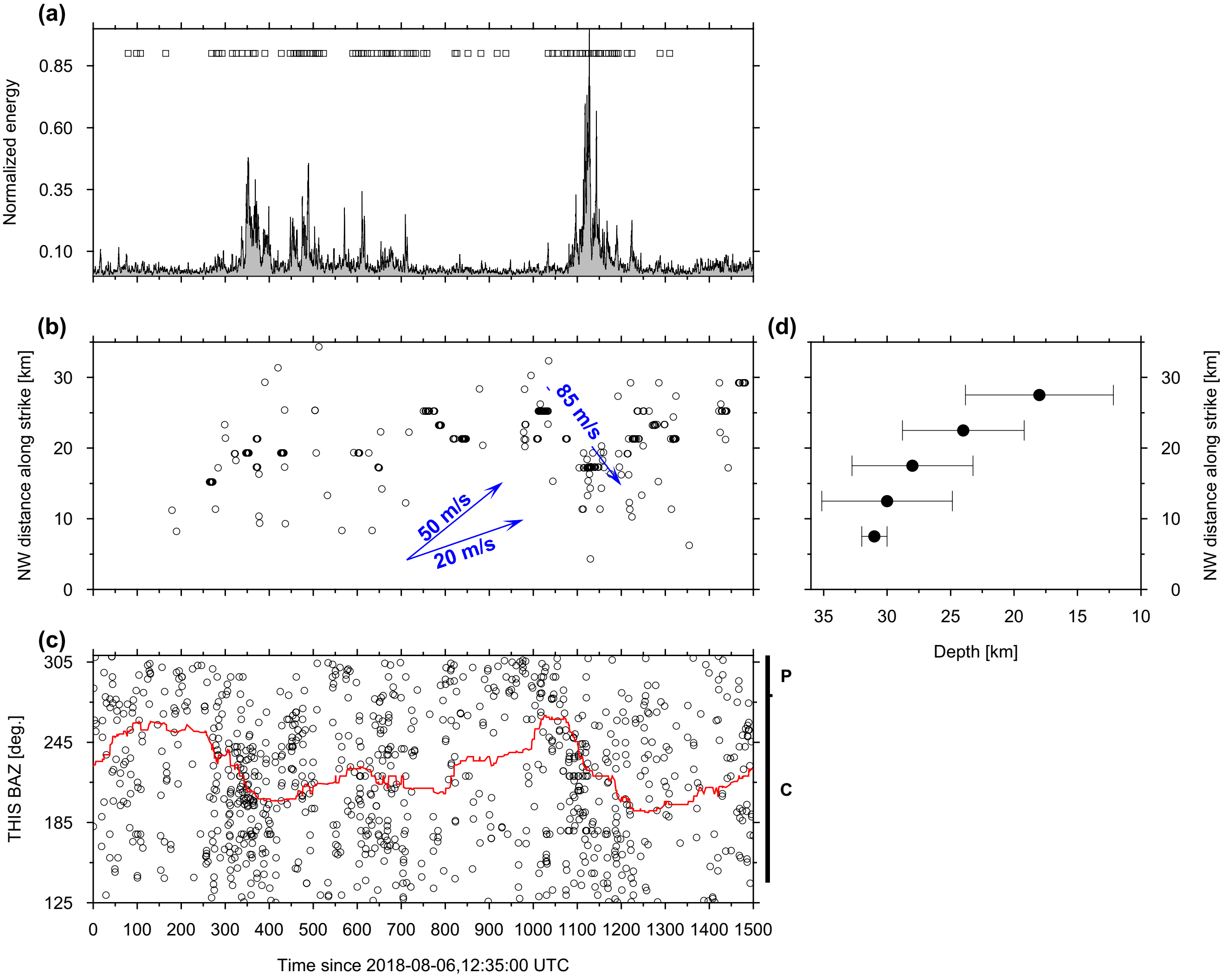

Figure 9. Rapid tremor migration along the Cholame section during a 25-min-long window containing tremor recorded on August 6, 2018. (a) Tremor envelope computed from 8 to 16 Hz vertical ground motion recorded at Plate Boundary Observatory (PBO) station B079. Low frequency earthquake (LFE) times are indicated by the squares at the top of the panel (b) Tremor location projected onto the SAF strike as a function of time. Arrows indicate southeast to northwest propagation velocities of 20–50 m/s, and northwest to southeast propagation velocities of 85 m/s. (c) Back azimuth as a function of time resolved at array THIS. The gray circles are for individual detections, and the red line is the median value computed for 100-s-long windows. Vertical bars indicate the extent of the Parkfield and Cholame sections, denoted by the letters P and C, respectively. (d) Median tremor depth as a function of along-strike distance.

shows data filtered between 8 and 16 Hz. Note that 8–16 Hz tremor energy recorded around 205–240 s is well above the noise level on all the borehole stations. This suggests that the Parkfield-Cholame borehole data set may be used to study the tremor source properties at frequencies higher than 10 Hz, above the upper cutoff frequency for most tremor-focused source studies.

The August 6 episode shown in Figures 8a and 8b originates primarily from the northern portion of the Cholame section, near the intersection with the SJFZ. Fletcher and Baker (2010) analyzed tremor signals originating from this area, and found two 1000-s-long tremor windows punctuated by short high-energy tremor bursts, which were correlated between the regional stations, and whose spectra were more broadband than the LFE spectra. We also observe such impulsive arrivals within the Cholame tremor. Using the results obtained from the borehole data, we inspected the frequency-dependent behavior of individual 2 s tremor bursts, and found some degree of variation in the ratio between 4 and 8 Hz and 8–16 Hz tremor energy. Because our detection criteria do not vary with frequency, and because the 8–16 Hz SNR is lower than the 4–8 Hz SNR, the number of detections drops with increasing frequency. However, we occasionally observe that the frequency-dependent radiation differs between consecutive bursts, causing systematic differences in locations obtained for each frequency band.

To better illustrate these differences, we show in Figure 8 the travel-time moveout curves (hyperbolas) for individual phases whose borehole network averaged C_{max} exceeds 0.3. Phases associated with 4–8 Hz tremors and 8–16 Hz tremors are indicated by the letters and *h*, respectively. Both panels show tremor depth is increasing with time. Initial phases (l_0 to l_3 and h_0 to h_3 in Figures 8a and 8b, respectively) are located at depth between 16 and 20 km, and later phases (l_6 to l_9 and h_6 to h_9 in Figures 8a and 8b, respectively) are located at depth of about 30 km. The depth increase is observed for both frequency bands, however the tremor depth imaged using the higher frequency range is monotonically increasing with time, while the lower frequency range show tremor depth is fluctuating during the interval containing the strongest arrivals (phases l_4 and l_5). This observation is reminiscent of the frequency-dependent radiation of large earthquake ruptures, during which low- and high-frequency radiators show little spatial overlap (e.g., Meng et al., 2011). Our results are also consistent with Fletcher and Baker (2010)'s inferences, who, based on particle motion analysis of high-amplitude, short-term tremor bursts, inferred the tremor source was migrating.

The along-depth migration that we resolve for this tremor burst is roughly 150 m/s, a factor of 6 faster than the fast LFE migrations reported by (Shelly, 2015). We also inferred similar values for tremor migrating along-depth during the August 5 episode (Figure 7b). Thus, similar to tremor observed in Cascadia, SAF tremor accompanying a several-days-long transient exhibits RTMs over short spatio-temporal scales. We further characterize the RTMs in Section 3.3 below. We also note that the LFE catalog contains 27 detections that are roughly synchronous with the strongest phases in Figure 8a. However, these events do not exhibit the short-term along-depth migration we observe, as they are mostly associated with a single LFE family whose depth is 21 km, and which is located less than 5 km southeast of the tremor source we identify.

The bottom panels in Figure 8 present in shades of red the distribution of tremor located using the borehole data set. We plot only detections whose C_{max} for frequencies <0.1 Hz and for frequencies >4 Hz is 6 and 15 times the median absolute deviation of each population. About 1% of the time windows we analyzed pass these criteria. In agreement with previous studies (Guo et al., 2017; H. Zhang et al., 2010), we find major tremor-producing areas in Parkfield and near the intersection between the SAF and the SJFZ. We also find that a considerable amount of tremor is occurring off the main SAF strand, with some episodes occurring along a 15-km-long section devoid of cataloged LFE activity north of Cholame (Figure 1). The location of activity is generally similar between the two frequency bands; however, we find that a few cells along the Parkfield section show more coherent activity in the 8–16 Hz band than in the 4–8 Hz band, demonstrated by a larger number of detections in the higher frequency band.

Figures 8c and 8d also show in open squares the August 5–9, 2018, LFE catalog locations and counts. We find that, while some of the LFE locations are correlated with tremor along the Cholame section, tremor locations are weakly correlated with LFEs in Parkfield, where abundant tremor signal is located off the main SAF strand. Note that, due to differences in the detection criteria, it is difficult to directly compare tremor and LFE counts in a given region. It is however possible to compare the relative distribution within each catalog, which yields poor agreement primarily north of Cholame. The error analysis presented in the supplementary materials suggests the horizontal error on temporally clustered tremor is about 5 km (Figure S4), which is smaller than the location discrepancies, thus allowing us to rule out factors such as the velocity model and station distribution used in the location procedure as being responsible for this result. Possible reasons for the discrepancies are further discussed below.

3.3. Observing and Characterizing RTM in Cholame

Analysis of the continuous multi-array data (Figure 4) and episodic tremor bursts observed on borehole sensors suggests Cholame tremor accompanying the August 2018 slow-earthquake exhibits steady along-strike propagation velocity of about 8 km/day between August 5 and 8. The slow along-strike migration is punctuated by high-frequency RTMs propagating along-depth at speeds of up to 150 m/s for short time intervals of up to about 100 s (Figures 8a and 8b).

Next, we demonstrate the 2018 transient also contains RTMs occurring over spatio-temporal scales that are considerably longer than the August 6 episode shown in Figures 8a and 8b. Figure 9 presents the analysis of a 25-min-long tremor window that was recorded by the local borehole network and the temporary arrays. Panel (a) presents the vertical seismic energy in the 8–16 Hz frequency range recorded at PBO borehole station B079. Panel (b) presents tremor locations obtained from the borehole data, which were projected onto the SAF strike. The vertical axis in Figure 9b corresponds to a portion of the SAF starting about 20 km southeast of the town of Cholame, and extending for 35 km to the northwest (Figure 1). Panel (c) presents the back azimuth resolved by array THIS located closest to the fault.

The locations we resolve clearly highlight rapid tremor migrating toward the northwest along the SAF strike for ~35 km, punctuated by two clear RTRs during which tremor propagates backwards toward an area that was previously ruptured during the same RTM. These trends are also consistent with the back azimuth resolved using the data recorded by array THIS (Figure 9c). At least two of the higher-amplitude tremor bursts associated with RTRs, are observed to propagate back toward the southeast at speeds of about 80 m/s. The first RTR is mostly observed on the array data between 200 and 400 s, and the second RTR is clearly observed by the array and borehole data between 1,000 and 1,200 s. Another short, low-amplitude RTR is observed on the borehole data between 700 and 850 s. The RTR resolved by the array and borehole datasets is associated with the strongest tremor energy during this RTM, and with the largest back-propagation distance. During the inter-RTR periods, tremor is observed to migrate more slowly along the fault's strike. The slow migration is most clearly observed on the array and borehole data between 400 and 1,000 s, and between 1,200 and 1,500 s. The reduction in amplitude is correlated with a decrease in the number of detections, and thus with overall reduction in the value of C_{max} before the RTR occurring around 1,100 s.

Figure 9d presents the median tremor depth computed for 5 km nonoverlapping bins along the fault's strike. We find that as the RTM progresses along strike its depth decreases from about 30 km to about 18 km. Most of the updip propagation takes place in the final 500 s, while the initial stage of the RTM is mostly confined to depths between 25 and 30 km. We note that the tremor depth reduction with progression in a northwesterly direction along strike is consistent with shallowing of LFE hypocenters along the same fault section (Figures 1b and 2). Assuming the scatter in tremor locations is representative of the dimensions of the rupture front, then, at its most energetic phases, the rupture is occupying an area whose length is less than 10 km and whose width is about 10 km.

The length and time scales characterizing this RTM are similar to the ones associated with RTMs observed during secondary slip fronts in Cascadia (Bletery et al., 2017; Hawthorne et al., 2016; Houston et al., 2011; Peng & Rubin, 2016). However, unlike the RTMs observed in Cascadia, which generally rupture only a small portion of the interface slipping during a major SSE (Hall et al., 2019; Rubin & Armbruster, 2013), the portion ruptured by the secondary front imaged here is more than half of the fault length ruptured during the entire 4-day transient. Since the August 6 burst shown in Figure 8 likely occurred before the major SSE front ruptured the northern terminus of the Cholame section (e.g., Figures 4a–4c), we infer that the secondary front travels well ahead of the main SSE rupture front.

Further inspection of the imaged RTM reveals the high level of complexity associated with the tremor source. As the secondary slip front migrates along-strike it is observed to activate isolated patches that produce prolonged sequences of tremor that remain spatially stationary. Such short-term stationary episodes can be clearly observed throughout the RTM, with longer sequences occurring after 700 s (Figure 9b). The stationary sources are sometimes characterized by high C_{max} values, and are generally coeval with intervals associated with high LFE rates.

4. Discussion

We utilize array and borehole data to resolve tremor locations along the SAF. Back projecting the array data onto the fault allows us to continuously track the tremor source during the August 2018 transient. A major advantage of the array technique employed here is that it allows us to determine the tremor epicentral location without using a detailed local velocity model. However, constraining the tremor depth does require that we project the maximal array coherency onto the fault by tracing rays resolved at the arrays through a local velocity model (e.g., Fletcher & Baker, 2010). Given the arrays configuration and SNR conditions, we believe this procedure will yield poorly constrained locations: the inter-array distances are shorter than the extent of the August 2018 SSE, such that the array data cannot provide good constraints on tremor depth for

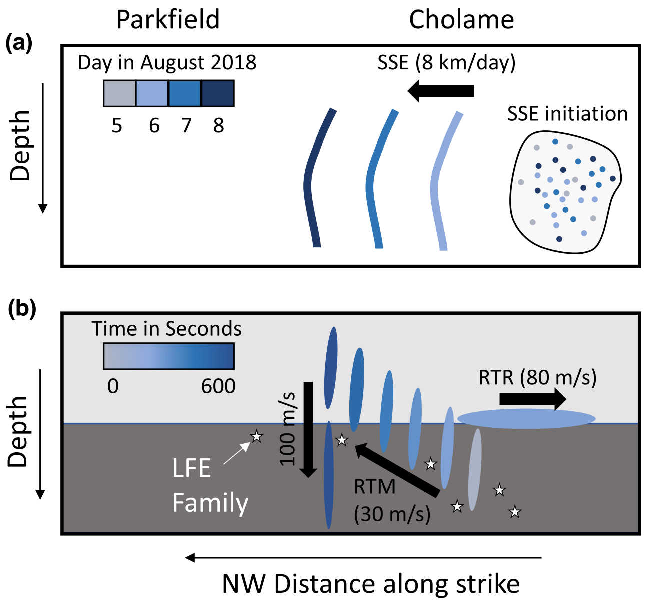

Figure 10. Schematic illustration of the styles of tremor migration observed during the August 2018 slow slip event (SSE), and the associated spatial and temporal scales. Colors indicate time, and colored regions denote areas delineated by tremor activity in different time windows. The arrows indicate propagation directions. (a) Initiation and long-term propagation of the SSE between August 5 and 8, 2018. Circles illustrate on-going activity in the initiation area along the central portion of the Cholame segment. (b) Short-term propagation during a 10-min-long Rapid Tremor Migration (RTM). Stars denote location of low frequency earthquake (LFE) families. Light gray rectangle indicate depth range devoid of LFE families, and dark gray rectangle indicate depth range associated with LFE families.

significant intervals of the 2018 August transient. We therefore utilize the borehole stations, which enable us to constrain the tremor locations during the entire duration of the August 2018 episode. Additionally, the superb SNR conditions of the borehole sites allow us to study tremor energy at frequencies >10 Hz, outside the range of most other tremor-focused studies. Thus the array and borehole analysis, together with the LFE catalog, complement each other and allow for improved understanding of the tremor activity.

4.1. Tremor Migration Style

We continuously analyzed the temporary array data to obtain high-resolution images of Cholame tremors. The analysis, confirmed by amplitudes of regional borehole records and LFE patterns, reveal a strong transient between August 5 and August 9, 2018. The styles of tremor migration we observed during the August 2018 SSE are shown schematically in Figure 10. The main front associated with this transient propagates at a velocity of about 8 km/day, comparable to previous estimates of slip transients inferred from the spatio-temporal analysis of LFEs (Shelly, 2017) or from tremor locations in Cascadia (Ghosh et al., 2009; Peng & Rubin, 2016) and Japan (Ito et al., 2007). The slow propagation is accompanied by on-going activity near the initiation area, close to the central-southern portion of the Cholame segment. Tremor amplitudes vary strongly during the transient, and include tens of short-term high-amplitude episodes whose durations are of the order of several hundreds of seconds. These episodes are characterized by rapid along-strike and along-depth propagation, and are referred to as RTMs. The highest propagation speeds are observed for along-depth (i.e., in the direction normal to the SSE slip vector) migration, which, during some bursts, may be as high as 150 m-per-second (Figures 7–9), about three orders of magnitude faster than the steady along-strike migration observed for the entire transient (Figure 4). Other episodes are characterized by along-strike propagation at speeds of 20–50 m/s for durations of several hundreds of seconds. Short intervals during these RTMs are associated with RTRs, during which the tremor front is observed to back-propagate for short distances (~10 km; Figure 9) into areas previously ruptured during the RTM. To the best of our knowledge, this is the first observation of RTRs along the Cholame-Parkfield section of the SAF. The short-term migration pattern often exhibits a systematic change with time on the temporary arrays and the regional borehole network, thereby ruling out the possibility that these observations are artifacts of the processing scheme.

While most of the > 4 Hz tremor energy is emitted from patches well below the bottom edge of the seismogenic zone, we locate intermittent bursts at shallower depths (sub panels in Figures 8c and 8d). Thus, Cholame tremor does appear to occasionally penetrate into the ~10-km-wide gap devoid of LFEs located directly below the seismogenic zone (Figure 1b). We do not find appreciable difference in the fault-normal distance and amplitude between these shallow and the deep tremors, or in their temporal distribution. It is possible that some tremors appear to be non-repeatable (and hence are not well detected by autocorrelation match filter techniques) due to near-fault attenuation structure reducing the LFEs energy level, or because of the sparsity of LFE sources in some areas.

4.2. Physical Constraints on the Tremor Source

The speed of short-term Cholame RTMs are up to an order of magnitude faster than RTMs often observed along the Cascadia subduction zone (Ghosh et al., 2010; Houston et al., 2011; Peng & Rubin, 2016; Rubin & Armbruster, 2013), or from the migration speeds inferred from LFE rates in Parkfield (Shelly, 2015). Additionally, Cholame RTMs are observed to rupture a significant portion of the fault slipping during the SSE. The area producing tremors during these RTMs occupies a band whose along-strike dimension is shorter than the total length ruptured during the entire burst (Figures 9a and 9b). Thus the geometry of the secondary front associated with the RTM might correspond to a narrow strain pulse traveling along the fault strike. The tremor depth distribution indicates the along-depth dimension of this pulse is ~10 km, and that it is bounded from above by the shallow seismogenic zone (Figure 9d). The tremor depth uncertainty relative to the width of the pulse makes it difficult to assess whether these are repeated ruptures of the same patch, or whether ruptures associated with the secondary slip fronts delineated by the RTMs are spatially complementary.

We are interested in placing constraints on the physics of the secondary fronts observed in Cholame. We follow Rubin and Armbruster (2013) and model the front as a finite strain pulse propagating in an elastic homogeneous medium, with total slip δ accumulating over length L. For simplicity, we assume that the stress drop over the region L is uniform. We further assume that $L < W$, with W being the downdip extent of the fault accommodating the SSE. The stress drop inside L is then given by:

$$\Delta\tau = \mu' c \frac{\delta}{L}, \tag{5}$$

where c is a geometric constant whose value is close to unity. For anti-plane shear $\mu' = \mu$, and for in-plane shear $\mu' = \mu/(1-\nu)$, where μ and ν are the shear modulus and Poisson's ratio, assumed equal to 30 GPa and 0.25, respectively.

The fault width W is derived from the distribution of tremor depths (Figures 8c and 8d) and its value is ~30 km. The pulse length L is estimated from the width of the band of active tremor during the RTM (Figure 9b), and its value lies between 5 and 10 km. Thus our assumption that $L < W$ seems reasonable given that the scatter in tremor locations likely obscures the actual dimension of L, and that L associated with coherent isolated stationary radiators is likely ~ 5 km. In this context, L refers to the distance between contemporaneous isolated stationary radiators, and not the size of the radiators themselves.

To proceed further, we need to come up with an estimate of δ, the average slip accumulated during a secondary front. The surface deformation associated with Parkfield transients is too small to be detected in individual geodetic records, but may be obtained by using more sophisticated processing techniques. By stacking multiple GPS time-series, and aligning them with respect to intervals with intense LFE activity, Rousset et al. (2019) revealed deep episodic fault slip beneath the Parkfield section with equivalent moment magnitude of M_w4.9. A similar magnitude was estimated from long-baseline strainmeter data for SSEs occurring along the deep extension of the SAF south of Cholame (Delbridge et al., 2020). Given the estimated geodetic moment, the amount of slip is dependent on the dimensions of the slipping region, which were constrained from the distribution of LFE families. For the fault dimension that is more compatible with our observations, Rousset et al. (2019) estimated 3.6 mm of cumulative slip per SSE. If we further assume that most of this slip is accumulated during the intervals containing the strongest tremors, then the amount of slip δ is equal to the total slip divided by n, where n is the number of resolved tremor bursts. For $n = 10$, $\delta \sim 0.03$ mm, and $\Delta\tau \sim 2$ kPa.

The stress drops we estimate are a factor of 4–5 smaller than the ones Rubin and Armbruster (2013) estimated for secondary fronts in Cascadia, and a factor of 2–3 smaller than the median value of secondary slip fronts associated with RTRs estimated by Bletery et al. (2017). One possible reason for this discrepancy is our estimate of the length scale L. For $L \sim 1$ km, which is similar to tremor width imaged by Rubin and Armbruster (2013), $\Delta\tau \sim 10$ kPa. However, obtaining locations with 1 km precision is at the resolution limit of our technique. Further analysis of coherent stationary tremor radiators (Figure 9b) may help address this issue. Note that for the simplified case assumed here, the tremor propagation speed is proportional to the ratio between the slip rate to the stress drop (e.g., Ampuero & Rubin, 2008). Since the slip rate we infer is of the same order as the one inferred for secondary fronts in Cascadia, the smaller stress drops in Cholame may account for the larger migration speeds observed there.

A second source of bias comes from the value of n, the number of bursts during which we assume significant slip is accumulated. One possibility, which is at odds with observations from Cascadia (e.g., Bartlow et al., 2011; Hawthorne & Rubin, 2013b; Wech et al., 2009), Japan (e.g., Obara, 2010), Alaska (Rousset et al., 2019), and Mexico (Frank, 2016), is that high rates of tremor in Cholame are simply not correlated with episodic deep fault slip. This possibility seems also to be at odds with the results of Rousset et al. (2019)

and Delbridge et al. (2020), suggesting the Parkfield geodetic signal and LFE activity are contemporaneous, and we consider it as unlikely. Another possibility is that some tremor goes undetected. If the number of secondary fronts is increased by a factor of 10, then stress drops for each secondary slip episode are expected to be of the order of a few hundred Pa. This is a plausible yet unlikely scenario. Analysis of tidal loading indicates Parkfield tremor activity is well correlated with semi-diurnal forcing by tidal shear-stress cycles (Thomas et al., 2009), suggesting the number of strong bursts associated with considerable aseismic strain release during the 4-day August 2018 transient is likely between 5 and 10.

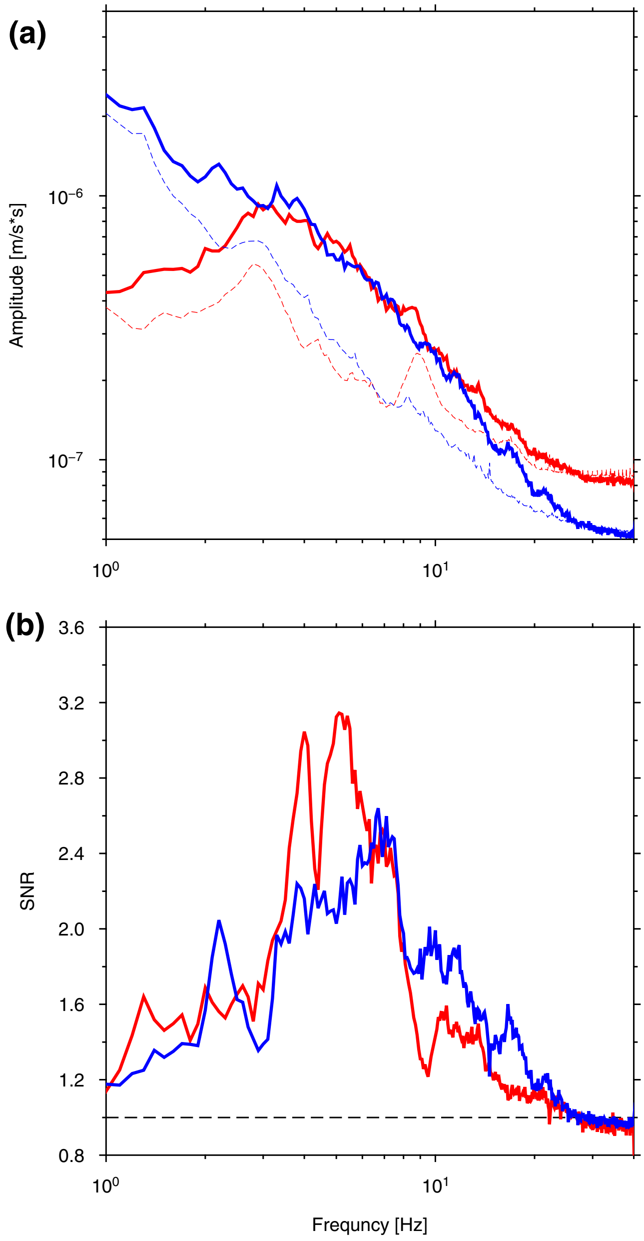

Figure 11. Spectra of vertical ground velocity recorded by regional borehole stations during Cholame and Parkfield tremor. Red and blue curves are for tremor originating from Cholame and Parkfield, respectively. Solid and dashed curves are for tremor and noise windows, respectively. (a) Tremor and noise spectra. (b) SNR. Dashed black line is for SNR = 1. Tremor spectra obtained by averaging 10 s windows from borehole data.

4.3. Comparison With the LFE Catalog

The spatio-temporal correlation between tremor and LFEs suggest they originate from a common source. However, much of Parkfield tremor is not associated with LFE activity (H. Zhang et al., 2010). Additionally, Parkfield LFEs are predominantly located on the fault, while some of the tremor apparently occurs off-fault (Guo et al., 2017). The August 2018 transient features tremors propagating both along the SAF strike and along its depth. The along-strike propagating is roughly consistent with the migration inferred from LFE activity. The distribution of tremor depth (8c,8d) suggest some of the episodes originate from areas devoid of LFE activity. The presence of these areas was previously suggested to be the result of a sharp reduction of fault strength due to near-lithostatic pore-pressure at the base of the crust (Gao & Wang, 2017). We observe that these gaps are not a permanent feature of the interface. Short episodes characterized by fast migration, which are associated with secondary fronts discussed above, are observed to intermittently migrate into these gaps. From bootstrap analysis (see Supporting Information S1), we estimate the absolute tremor location uncertainty is a few km, smaller than the spatial bins used in Figures 8c and 8d. The spatial consistency of temporally clustered tremor bursts and the high coherency they exhibit suggest the uncertainty on the relative locations is small.

LFE rates also increase in the August 5–8 time window, and their catalog suggests simultaneous activation of the Cholame and Parkfield sections. However, there are notable discrepancies between the spatio-temporal evolution of LFEs and tremor in Parkfield. These discrepancies may be partly due to SNR conditions. Our analysis suggests the borehole SNR in the 2–6 Hz band is higher for Cholame tremors, while the borehole SNR in the >6 Hz band is higher for Parkfield tremors (Figure 11). Although the high-frequency fall-off rate for Parkfield tremor signals is larger than for Cholame, the >6 Hz noise level in the Parkfield area is lower, facilitating high-frequency envelope-based detection in that area. Additionally, the amplitude of Cholame's LFEs is considerably higher than Parkfield's LFEs (Shelly, 2017, Figure 1c), likely reflecting the improved SNR in the 2–6 Hz frequency band observed in that area (bottom panel in Figure 11).

A second factor affecting the LFE counts involves their detection procedure, which requires the network-averaged coherency between a master-template and the seismogram to exceed a pre-defined threshold. In the cases where LFE lag times are shorter than the duration of the template, multiple phases arriving within the LFE template window are expected to reduce the correlation. These arrivals are expected to show as spectral peaks with period corresponding to integer multiples of the inverse of the inter LFE-times (Gomberg et al., 2016). However, as long as the lateral extent of the tremor-producing area is small compared to the network aperture, this phenomenon should not affect the maximal borehole network-averaged phase coherency; in this case, the location associated with C_{max} may reflect the (weighted) mean location of a cluster of asperities whose slips produce the observed tremor burst.

4.4. Frequency-Dependent Radiation During Episodic Tremor and Comparison With Previous Studies

Recent observations from the Nankai subduction zone (Kaneko et al., 2018; Masuda et al., 2020) and from Cascadia (Ide, 2019), suggest that seismic slip in the 0.1–10 Hz frequency range that accompanies slow ruptures represent a continuous, broadband phenomena. However, locating these sources is hampered by poor signal-to-noise ratio (SNR) conditions.

We apply our technique to characterize $>$ 4 Hz radiation during Parkfield tremor bursts. We find that tremor energy at frequencies as high as 16 Hz is coherent across the borehole network. Thus, the >10 Hz SNR for Parkfield and Cholame tremor recorded by the borehole stations is higher than the SNR for tremor in Cascadia recorded by surface stations over a similar frequency range (e.g., J. Zhang et al., 2011, Figure 3). The presence of high-frequency tremor signals in Parkfield was also observed by Guilhem and Nadeau (2012), however their envelope processing methodology did not have sufficient resolution for determining the locations of individual high-frequency tremor bursts often occurring within a 100-s-long tremor window.

Frequency-dependent radiation was observed during large earthquake ruptures (Nakahara, 2008; Meng et al., 2011), and recently also during slow ruptures occurring in subduction zones (Kaneko et al., 2018), and is important for elucidating the physics of slow ruptures (Ide, 2019). Our observations suggest that high- and low-frequency tremor energies within a given tremor episode may sometimes exhibit spatially complementary behavior. We also observe that some areas produce more coherent tremor at higher frequencies than others. Thus, the tremor wavefield is observed to contain incoherent and coherent components, with the latter often associated with LFEs, or, as in Fletcher and Baker (2010)'s and in this study, with impulsive, possibly shear-slip sources. Our analysis suggests these counterparts are activated simultaneously. Further investigation is required in order to assess the effects of inelastic attenuation and structural heterogeneity along the raypath on these observations, however the consistency of temporally clustered tremor radiation indicates the locations are not very affected by the SNR or the processing scheme.

Our results can be compared to the ones obtained by Fletcher and Baker (2010) and Ryberg et al. (2010). Fletcher and Baker (2010) found high-amplitude, short-term bursts within 1000-s-long tremor episodes which were correlated among the regional stations, and whose polarity and spectral properties were compatible with *S*-waves emitted from an impulsive shear-slip source whose approximated magnitude is $M = 0.3$. Spectral analysis of the short-term bursts indicates they are enriched in 4 Hz energy relative to microearthquakes with similar magnitudes, which may be due to the movement of fluids or gas in the tremorgenic area (Fletcher & McGarr, 2011). Note that the 4 Hz peak is absent from the spectra shown in Figures 11a because these spectra were computed for 10-s-long tremor windows, many of which are not associated with the short-term bursts discussed by Fletcher and Baker (2010) and Fletcher and McGarr (2011).

Fletcher and Baker (2010) analyzed data from a single array to determine the Cholame tremor source location, which yielded depth estimates that are not very well constrained. Additionally, they constrained the source locations to lie along the SAF trace. The uncertainty associated with their locations was mostly the result of the limited azimuthal coverage, as well as the lack of deep well-located sources required to calibrate the UPSAR apparent velocity estimates. Our methodology circumvents some of these issues, at the expense of analyzing signal envelopes rather than the raw data. However, as demonstrated here (i.e., Figures 8 and 9), the improved station coverage and SNR conditions at the boreholes more than offset the loss of phase information involved in enveloping the signal.

Ryberg et al. (2010) located tremor signals in Cholame using three arrays located near the fault. They resolved tremor migrating along the SAF strike at speeds that vary between 8 and 26 m/s, slightly slower than the range of speeds we observe during along-strike propagation (Figure 9), and considerably slower than speeds estimated during along-depth propagation (Figure 8). Ryberg et al. (2010)'s array-based locations lie mostly off the SAF trace, at a distance of ~10 km southwest of the SAF, near the intersection with the SJFZ (Figure 1a). These locations were then corrected by assuming tremors were co-located with previously determined LFE families on the SAF trace. In this study, we did not impose such constraints on the tremor source, yet were able to fit the signal travel times across stations tens of km apart (Figures 8a and 8b). The observation that the source systematically migrates in the along-depth and along-strike directions (Figures 8b and 9a), while exhibiting C_{max} values that mostly lie between 0.3 and 0.6 (Figure 9c), suggests the uncertainties associated with the velocity model or artifacts in the back-projection procedure are small. We attribute this result to the spatial coverage and high SNR of the borehole stations relative to the surface array records used here or by Ryberg et al. (2010).

5. Conclusions

In order to study tremor and LFEs, we deployed three dense seismic arrays near the Cholame section of the SAF in central CA. The arrays recorded a 4-day-long transient slip event, which occurred between August 5and 9, 2018. The event was accompanied by high-amplitude tremors and LFEs, which were observed across the regional network and the temporary arrays.

We calibrate the slowness resolved at the arrays using well-located regional earthquakes. The deviations between the true and apparent back azimuth for sites separated by over 10 km exhibit similar azimuthal dependence. This suggests a large-scale velocity anomaly, which refracts rays impinging on the arrays. Assuming a simplified geometry, we estimate the deep reflector strikes at a high angle to and crosses the SAF in that area.

We use the array data to continuously track the tremor as it migrates along the SAF strike during the first days of August 2018. The tremor is observed to migrate both along-strike and along-depth at velocities that vary by three orders of magnitude. The main slow slip front initiates south of Cholame. The initiation area remains active, while the tremor propagates toward the northwest at a speed of about 8 km/day. Using high-resolution borehole data, we also observe secondary slip fronts which are marked by rapid tremor propagating at speeds of up to 100 m/s. Most of the rapid migrations propagate from southeast to the northwest, however, we also observe some back-propagating fronts rerupturing fault portions that extend for several kilometers behind the main tremor front. Episodic tremor is observed to migrate into areas devoid of LFE activity, including a 5–10 km gap below the seismogenic zone and a 15 km portion of the SAF between Cholame and Parkfield.

By using near-fault borehole data, we obtain high-resolution images of the secondary fronts. We find that they may initiate behind the main slow front and travel ahead of it. The location of tremor delineating these secondary fronts suggests they are associated with a narrow slip pulse bounded from above by the seismogenic zone. We use the tremor locations to constrain the dimensions of the pulse, and estimate that the stress drop associated with the migrating pulse is of the order of a few kPa.

Appendix A: Constraints on Regional Structure From Back Azimuth Measurements

Using dense array and borehole network data, we identify and characterize tremor activity along the Cholame and Parkfield sections of the SAF. The slowness resolved by the arrays deviates from the true slowness associated with wavefronts due to regional earthquakes. We obtain empirical correction terms by analyzing arrivals from multiple earthquakes. Assuming a 1-D velocity model, the deviation from the true back azimuth may be attributed to a reflector striking at a high angle to the SAF. Determining the depth extent of this reflector requires a detailed knowledge of the shallow velocity structure, and is beyond the scope of this paper. We note that off fault deformation associated with the SAF in that area has resulted in multiple anticlines that are sub-parallel to the fault's strike (Mount & Suppe, 1987), as well as with shorter strike-slip faults southwest of the SAF that are oblique to the SAF strike (Titus et al., 2011). Rays refracted from these structures may cause the apparent slowness to deviate from the true slowness. However, the orientation of the reflector we infer from the array measurements is nearly normal to the SAF strike, and thus it is unlikely the result of refraction due to the structures highlighted by Mount and Suppe (1987). Previous analysis performed by Fletcher et al. (2006) and Meng et al. (2014) using the U.S. Geological Survey Parkfield Seismic Array (UPSAR) data recorded 8 km to the west of the SAF and 18 km north-northwest of site TCHL, also yields a significant bias in apparent back azimuth. This was proposed to be the result of rays bending within a fast near-vertical layer bordering the fault core to the southwest (Fletcher et al., 2006), or as the result of a shallow reflector striking parallel to the SAF (Meng et al., 2014). Our observation, which is consistent between the three arrays, suggests the length scale associated with the perturbation in the velocity structure is of the order of tens of kilometers, and extends across the fault from southwest to the northeast. This geometry is perhaps more compatible with a deep anomaly, similar to the one previously imaged by magnetotelluric data (Becken et al., 2011), in regional 3-D velocity models (Zeng et al., 2016), and in deep reflection imaging (Bleibinhaus et al., 2007). We note that determining the geometry of this deep anomaly may be obtained by using the regional network to estimate the spatial distribution of the deviations between the apparent and true back azimuth measurements, which could then be mapped onto the structure via a forward 2-D ray tracing procedure.

Data Availability Statement

The Cholame array data are available at the following doi: https://www.fdsn.org/networks/detail/1B_2018/. Data used in this study were recorded and maintained by the following networks: the Northern California Seismic Network (doi: http://www.fdsn.org/datacenters/detail/NCEDC/), the Plate Boundary Observatory Borehole Seismic Network (doi: http://www.fdsn.org/networks/detail/PB), IRIS (doi: https://www.fdsn.org/networks/detail/II/), and Tremorscope (doi: http://seismo.berkeley.edu/research/tremorscope.html).

Acknowledgments
The authors thank Mr. Daniel Sinton and Mr. Pete Clark for granting permissions to deploy the arrays on their property. They thank D. Shelly for providing the LFE catalog used in this study. The comments provided by two anonymous reviewers significantly improved the quality of this manuscript. The research was supported by BSF grant #2018353.

References

Ampuero, J.-P., & Rubin, A. M. (2008). Earthquake nucleation on rate and state faults: Aging and slip laws. *Journal of Geophysical Research*, *113*(B1). https://doi.org/10.1029/2007JB005082

Bartlow, N. M., Miyazaki, S., Bradley, A. M., & Segall, P. (2011). Space-time correlation of slip and tremor during the 2009 Cascadia slow slip event. *Geophysical Research Letters*, *38*(18). https://doi.org/10.1029/2011GL048714

Becken, M., Ritter, O., Bedrosian, P. A., & Weckmann, U. (2011). Correlation between deep fluids, tremor and creep along the central San Andreas fault. *Nature*, *480*(7375), 87–90. https://doi.org/10.1038/nature10609

Beroza, G. C., & Ide, S. (2011). Slow Earthquakes and Nonvolcanic Tremor. *Annual Review of Earth and Planetary Sciences*, *39*(1), 271–296. https://doi.org/10.1146/annurev-earth-040809-152531

Bleibinhaus, F., Hole, J. A., Ryberg, T., & Fuis, G. S. (2007). Structure of the California Coast Ranges and San Andreas Fault at SAFOD from seismic waveform inversion and reflection imaging. *Journal of Geophysical Research*, *112*(B6), 315. https://doi.org/10.1029/2006JB004611

Bletery, Q., Thomas, A. M., Hawthorne, J. C., Skarbek, R. M., Rempel, A. W., & Krogstad, R. D. (2017). Characteristics of secondary slip fronts associated with slow earthquakes in Cascadia. *Earth and Planetary Science Letters*, *463*, 212–220. https://doi.org/10.1016/J.EPSL.2017.01.046

Bondár, I., North, R. G., & Beall, G. (1999). Teleseismic slowness-azimuth station corrections for the international monitoring system seismic network. *Bulletin of the Seismological Society of America*, *89*, 989–1003. https://doi.org/10.1785/bssa0890040989

Bostock, M. G., Royer, A. A., Hearn, E. H., & Peacock, S. M. (2012). Low frequency earthquakes below southern Vancouver Island. *Geochemistry, Geophysics, Geosystems*, *13*(11). https://doi.org/10.1029/2012GC004391

Bürgmann, R. (2018). The geophysics, geology and mechanics of slow fault slip. *Earth and Planetary Science Letters*, *495*, 112–134. https://doi.org/10.1016/J.EPSL.2018.04.062

Chave, A. D., Thomson, D. J., & Ander, M. E. (1987). On the robust estimation of power spectra, coherences, and transfer functions. *Journal of Geophysical Research*, *92*(B1), 633. https://doi.org/10.1029/JB092iB01p00633

Delbridge, B. G., Carmichael, J. D., Nadeau, R. M., Shelly, D. R., & Bürgmann, R. (2020). Geodetic measurements of slow-slip events southeast of Parkfield, CA. *Journal of Geophysical Research*, *125*(5). https://doi.org/10.1029/2019JB019059

Flanagan, M. P., Myers, S. C., & Simmons, N. A. (2012). *Model-based corrections to observed back azimuth and slowness observations from a dipping Mohorovicic discontinuity, tech. rep*. Albuquerque. Monitoring Research Review.

Fletcher, J. B., & Baker, L. M. (2010). Analysis of nonvolcanic tremor on the San Andreas Fault near Parkfield, CA using U. S. Geological Survey Parkfield seismic array. *Journal of Geophysical Research*, *115*(B10). https://doi.org/10.1029/2010JB007511

Fletcher, J. B., & McGarr, A. (2011). Moments, magnitudes, and radiated energies of non-volcanic tremor near Cholame, CA, from ground motion spectra at UPSAR. *Geophysical Research Letters*, *38*(16). https://doi.org/10.1029/2011GL048636

Fletcher, J. B., Spudich, P., & Baker, L. M. (2006). Rupture propagation of the 2004 Parkfield, California, earthquake from observations at the UPSAR. *Bulletin of the Seismological Society of America*, *96*(4B), 129–S142. https://doi.org/10.1785/0120050812

Frank, W. B. (2016). Slow slip hidden in the noise: The intermittence of tectonic release. *Geophysical Research Letters*, *43*(19), 10125–10133. https://doi.org/10.1002/2016GL069537

Frank, W. B., & Shapiro, N. M. (2014). Automatic detection of low-frequency earthquakes (LFEs) based on a beamformed network response. *Geophysical Journal International*, *197*(2), 1215–1223. https://doi.org/10.1093/gji/ggu058

Gao, X., & Wang, K. (2017). Rheological separation of the megathrust seismogenic zone and episodic tremor and slip. *Nature*, *543*(7645), 416–419. https://doi.org/10.1038/nature21389

Ghosh, A., Vidale, J. E., Sweet, J. R., Creager, K. C., & Wech, A. G. (2009). Tremor patches in Cascadia revealed by seismic array analysis. *Geophysical Research Letters*, *36*. https://doi.org/10.1029/2009GL039080

Ghosh, A., Vidale, J. E., Sweet, J. R., Creager, K. C., Wech, A. G., Houston, H., & Brodsky, E. E. (2010). Rapid, continuous streaking of tremor in Cascadia. *Geochemistry, Geophysics, Geosystems*, *11*(12). https://doi.org/10.1029/2010GC003305

Gibbons, S. J., & Ringdal, F. (2006). The detection of low magnitude seismic events using array-based waveform correlation. *Geophysical Journal International*, *165*(1), 149–166. https://doi.org/10.1111/j.1365-246X.2006.02865.x

Gomberg, J., Agnew, D. C., & Schwartz, S. Y. (2016). Alternative source models of very low frequency events. *Journal of Geophysical Research*, *121*(9), 6722–6740. https://doi.org/10.1002/2016JB013001

Guilhem, A., & Nadeau, R. M. (2012). Episodic tremors and deep slow-slip events in Central California. *Earth and Planetary Science Letters*, *357–358*, 1–10. https://doi.org/10.1016/J.EPSL.2012.09.028

Guo, H., Zhang, H., Nadeau, R. M., & Peng, Z. (2017). High-resolution deep tectonic tremor locations beneath the San Andreas Fault near Cholame, California, using the double-pair double-difference location method. *Journal of Geophysical Research*, *122*(4), 3062–3075. https://doi.org/10.1002/2016JB013919

Hall, K., Schmidt, D., & Houston, H. (2019). Peak tremor rates lead peak slip rates during propagation of two large slow earthquakes in Cascadia. *Geochemistry, Geophysics, Geosystems*, *20*(11), 4665–4675. https://doi.org/10.1029/2019GC008510

Hawthorne, J., & Ampuero, J.-P. (2017). A phase coherence approach to identifying co-located earthquakes and tremor. *Geophysical Journal International*, *209*(2), ggx012. https://doi.org/10.1093/gji/ggx012

Hawthorne, J. C., Bostock, M. G., Royer, A. A., & Thomas, A. M. (2016). Variations in slow slip moment rate associated with rapid tremor reversals in cascadia. *Geochemistry, Geophysics, Geosystems*, *17*(12), 4899–4919. https://doi.org/10.1002/2016gc006489

Hawthorne, J. C., & Rubin, A. M. (2013a). Tidal modulation and back-propagating fronts in slow slip events simulated with a velocity-weakening to velocity-strengthening friction law. *Journal of Geophysical Research*, *118*(3), 1216–1239. https://doi.org/10.1002/jgrb.50107

Hawthorne, J. C., & Rubin, A. M. (2013b). Short-time scale correlation between slow slip and tremor in Cascadia. *Journal of Geophysical Research*, *118*(3), 1316–1329. https://doi.org/10.1002/jgrb.50103

Houston, H., Delbridge, B. G., Wech, A. G., & Creager, K. C. (2011). Rapid tremor reversals in Cascadia generated by a weakened plate interface. *Nature Geoscience*, *4*(6), 404–409. https://doi.org/10.1038/ngeo1157

Ide, S. (2019). Detection of low-frequency earthquakes in broadband random time sequences: Are they independent events? *Journal of Geophysical Research*, *124*(8), 8611–8625. https://doi.org/10.1029/2019JB017643

Inbal, A., Ampuero, J.-P., & Clayton, R. (2016). Localized seismic deformation in the upper mantle revealed by dense seismic arrays. *Science*, *354*(6308), 88–92. https://doi.org/10.1126/science.aaf1370

Inbal, A., Clayton, R., & Ampuero, J.-P. (2015). Imaging widespread seismicity at midlower crustal depths beneath Long Beach, CA, with a dense seismic array: Evidence for a depth-dependent earthquake size distribution. *Geophysical Research Letters*, *42*(15), 6314–6323. https://doi.org/10.1002/2015GL064942

Inbal, A., Cristea-Platon, T., Ampuero, J.-P., Hillers, G., Agnew, D., & Hough, S. E. (2018). Sources of long-range anthropogenic noise in Southern California and implications for tectonic tremor detection. *Bulletin of the Seismological Society of America*, *108*(6), 3511–3527. https://doi.org/10.1785/0120180130

Ito, Y., Obara, K., Shiomi, K., Sekine, S., & Hirose, H. (2007). Slow earthquakes coincident with episodic tremors and slow slip events. *Science*, *315*(5811), 503–506. https://doi.org/10.1126/science.1134454

Johnson, C. W., Meng, H., Vernon, F., & Ben-Zion, Y. (2019). Characteristics of ground motion generated by wind interaction with trees, structures, and other surface obstacles. *Journal of Geophysical Research*, *124*(8), 8519–8539. https://doi.org/10.1029/2018JB017151

Kaneko, L., Ide, S., & Nakano, M. (2018). Slow earthquakes in the microseism frequency band (0.1-1.0 Hz) off Kii Peninsula, Japan. *Geophysical Research Letters*, *45*(6), 2618–2624. https://doi.org/10.1002/2017GL076773

Karplus, M., & Schmandt, B. (2018). Preface to the focus section on geophone array seismology. *Seismological Research Letters*, *89*(5), 1597–1600. https://doi.org/10.1785/0220180212

Luo, Y., & Ampuero, J.-P. (2018). Stability of faults with heterogeneous friction properties and effective normal stress. *Tectonophysics*, *733*, 257–272. https://doi.org/10.1016/J.TECTO.2017.11.006

Masuda, K., Ide, S., Ohta, K., & Matsuzawa, T. (2020). Bridging the gap between low-frequency and very-low-frequency earthquakes. *Earth Planets and Space*, *72*(1), 47. https://doi.org/10.1186/s40623-020-01172-8

Meng, H., & Ben-Zion, Y. (2018). Characteristics of Airplanes and helicopters recorded by a dense seismic array near Anza California. *Journal of Geophysical Research: Solid Earth*, *123*(6), 4783–4797. https://doi.org/10.1029/2017JB015240

Meng, L., Allen, R. M., & Ampuero, J.-P. (2014). Application of seismic array processing to earthquake early warning. *Bulletin of the Seismological Society of America*, *104*(5), 2553–2561. https://doi.org/10.1785/0120130277

Meng, L., Inbal, A., & Ampuero, J.-P. (2011). A window into the complexity of the dynamic rupture of the 2011 Mw 9 Tohoku-Oki earthquake. *Geophysical Research Letters*, *38*(16), a–n. https://doi.org/10.1029/2011GL048118

Mount, V. S., & Suppe, J. (1987). State of stress near the San Andreas Fault: Implications for wrench tectonics. *Geology*, *15*(12), 1143. https://doi.org/10.1130/0091-7613(1987)15<1143:sosnts>2.0.co;2

Nakahara, H. (2008). Seismogram envelope inversion for high-frequency seismic energy radiation from moderate-to-large earthquakes. *Advances in Geophysics*, *50*, 401–426. https://doi.org/10.1016/S0065-2687(08)00015-0

Niazi, I. (1966). Corrections to apparent azimuths and travel-time gradients for a dipping mohorovich discontinuity. *The Bulletin of the Seismological Society of America*, *56*, 491–509. https://doi.org/10.1785/BSSA0560020491

Obara, K. (2002). Nonvolcanic deep tremor associated with subduction in southwest Japan. *Science*, *296*(5573), 1679–1681. https://doi.org/10.1126/science.1070378

Obara, K. (2010). Phenomenology of deep slow earthquake family in southwest Japan: Spatiotemporal characteristics and segmentation. *Journal of Geophysical Research*, *115*(B8), B00A25. https://doi.org/10.1029/2008JB006048

Obara, K., Matsuzawa, T., Tanaka, S., & Maeda, T. (2012). Depth-dependent mode of tremor migration beneath Kii Peninsula, Nankai subduction zone. *Geophysical Research Letters*, *39*(10), a–n. https://doi.org/10.1029/2012GL051420

Peng, Y., & Rubin, A. M. (2016). High-resolution images of tremor migrations beneath the Olympic Peninsula from stacked array of arrays seismic data. *Geochemistry, Geophysics, Geosystems*, *17*(2), 587–601. https://doi.org/10.1002/2015GC006141

Peng, Z., & Gomberg, J. (2010). An integrated perspective of the continuum between earthquakes and slow-slip phenomena. *Nature Geoscience*, *3*(9), 599–607. https://doi.org/10.1038/ngeo940

Riahi, N., & Gerstoft, P. (2017). Using graph clustering to locate sources within a dense sensor array. *Signal Processing*, *132*, 110–120. https://doi.org/10.1016/J.SIGPRO.2016.10.001

Rousset, B., Bürgmann, R., & Campillo, M. (2019). Slow slip events in the roots of the San Andreas Fault. *Science Advances*, *5*(2), eaav3274. https://doi.org/10.1126/sciadv.aav3274

Rubin, A. M. (2011). Designer friction laws for bimodal slow slip propagation speeds. *Geochemistry, Geophysics, Geosystems*, *12*(4). https://doi.org/10.1029/2010GC003386

Rubin, A. M., & Armbruster, J. G. (2013). Imaging slow slip fronts in Cascadia with high precision cross-station tremor locations. *Geochemistry, Geophysics, Geosystems*, *14*(12), 5371–5392. https://doi.org/10.1002/2013GC005031

Ryberg, T., Haberland, C., Fuis, G. S., Ellsworth, W. L., & Shelly, D. R. (2010). Locating non-volcanic tremor along the San Andreas Fault using a multiple array source imaging technique. *Geophysical Journal International*, *183*(3), 1485–1500. https://doi.org/10.1111/j.1365-246X.2010.04805.x

Savard, G., & Bostock, M. G. (2015). Detection and location of low-frequency earthquakes using cross-station correlation. *Bulletin of the Seismological Society of America*, *105*(4), 2128–2142. https://doi.org/10.1785/0120140301

Shelly, D. R. (2015). Complexity of the deep San Andreas Fault zone defined by cascading tremor. *Nature Geoscience*, *8*(2), 145–151. https://doi.org/10.1038/ngeo2335

Shelly, D. R. (2017). A 15 year catalog of more than 1 million low-frequency earthquakes: Tracking tremor and slip along the deep San Andreas Fault. *Journal of Geophysical Research*, *122*(5), 3739–3753. https://doi.org/10.1002/2017JB014047

Shelly, D. R., Beroza, G. C., & Ide, S. (2007). Non-volcanic tremor and low-frequency earthquake swarms. *Nature*, *446*(7133), 305–307. https://doi.org/10.1038/nature05666

Shelly, D. R., Beroza, G. C., Ide, S., & Nakamula, S. (2006). Low-frequency earthquakes in Shikoku, Japan, and their relationship to episodic tremor and slip. *Nature*, *442*(7099), 188–191. https://doi.org/10.1038/nature04931

Thomas, A. M., Beeler, N. M., Bletery, Q., Burgmann, R., & Shelly, D. R. (2018). Using low-frequency earthquake families on the San Andreas Fault as deep creepmeters. *Journal of Geophysical Research*, *123*(1), 457–475. https://doi.org/10.1002/2017JB014404

Thomas, A. M., & Bostock, M. G. (2015). Identifying low-frequency earthquakes in central Cascadia using cross-station correlation. *Tectonophysics*, *658*, 111–116. https://doi.org/10.1016/J.TECTO.2015.07.013

Thomas, A. M., Nadeau, R. M., & Bürgmann, R. (2009). Tremor-tide correlations and near-lithostatic pore pressure on the deep San Andreas Fault. *Nature*, *462*(7276), 1048–1051. https://doi.org/10.1038/nature08654

Thurber, C., Zhang, H., Waldhauser, F., Hardebeck, J., Michael, A., & Eberhart-Phillips, D. (2006). Three-dimensional compressional wavespeed model, earthquake relocations, and focal mechanisms for the Parkfield, California, Region. *Bulletin of the Seismological Society of America*, *96*(4B), S38–S49. https://doi.org/10.1785/0120050825

Titus, S. J., Dyson, M., DeMets, C., Tikoff, B., Rolandone, F., & Burgmann, R. (2011). Geologic versus geodetic deformation adjacent to the San Andreas fault, central California. *The Geological Society of America Bulletin*, *123*(5–6), 794–820. https://doi.org/10.1130/B30150.1

Wech, A. G., & Creager, K. C. (2008). Automated detection and location of Cascadia tremor. *Geophysical Research Letters*, *35*(20), L20. https://doi.org/10.1029/2008GL035458

Wech, A. G., Creager, K. C., & Melbourne, T. I. (2009). Seismic and geodetic constraints on Cascadia slow slip. *Journal of Geophysical Research*, *114*(B10). https://doi.org/10.1029/2008JB006090

Zeng, X., Thurber, C. H., Shelly, D. R., Harrington, R. M., Cochran, E. S., Bennington, N. L., et al. (2016). 3-D *P*- and *S*-wave velocity structure and low-frequency earthquake locations in the Parkfield, California region. *Geophysical Journal International*, *206*(3), 1574–1585. https://doi.org/10.1093/gji/ggw217

Zhang, H., Nadeau, R. M., & Toksoz, M. N. (2010). Locating nonvolcanic tremors beneath the San Andreas Fault using a station-pair double-difference location method. *Geophysical Research Letters*, *37*(13). https://doi.org/10.1029/2010GL043577

Zhang, J., Gerstoft, P., Shearer, P. M., Yao, H., Vidale, J. E., Houston, H., & Ghosh, A. (2011). Cascadia tremor spectra: Low corner frequencies and earthquake-like high-frequency falloff. *Geochemistry, Geophysics, Geosystems*, *12*(10). https://doi.org/10.1029/2011GC003759